SLAC-PROPOSAL-E161
Sept. 8, 2000

Proposal to Measure The Gluon Spin Distribution Using Polarized Open Charm Photoproduction

V. Ghazikhanian, G. Igo, S. Trentalange
University of California Los Angeles, Los Angeles CA 90095

S. Bueltmann
Jefferson Lab, Newport News VA 23606

G. Court
University of Liverpool, Liverpool L69 3BX, United Kingdom

S. Penttila, G. Mitchell
Los Alamos National Laboratory, Los Alamos, New Mexico 87545

R. G. Arnold, P. E. Bosted(*), R. Hicks, R. Miskimen, G. Peterson, S. E. Rock(+), J. Shaw
University of Massachusetts, Amherst, Massachusetts 01003
(*) co-spokesperson (contact: Bosted@Slac.Stanford.Edu (413) 545-2011)
(+) contact person at SLAC (contact: ser@Slac.Stanford.Edu (650) 926-3454)

R. Lombard
DAPNIA-Service de Physique Nucleaire Centre d'Etudes de Saclay, F–91191 Gif/Yvette, France

G. Tamas
Institut fur Kernphysik, D55099 Mainz, Germany

A. Klein, S. Kuhn, C. Hyde-Wright, L. M. Qin
Old Dominion University, Norfolk, Virginia 23529

St. Goertz, W. Meyer, G. Reicherz
Ruhr-UniversitBochum, Universitstr 150, Bochum, Germany

P. Decowski
Smith College, Northampton, Massachusetts 01063

P. Anthony, R. Erickson, T. Fieguth,
S. Rokni, S. St.Lorant, Z. M. Szalata, D. Walz, M. Woods
Stanford Linear Accelerator Center, Stanford, California 94309

D. Crabb(*), D. Day, R. Lindgren, D. Pocanic, O. Rondon, F. Wesselmann
University of Virginia, Charlottesville, Virginia 22901
(*) co-spokesperson (contact: Dgc3q@Virginia.Edu (804) 924-6790)

D. Armstrong, T. Averett, K. Griffioen
College of William and Mary, Williamsburg, Virginia 23187

N. Akopov, A. Apyan, R. Avakian, A. Avetisian, S. Darbinian, K. Ispirian, S. Taroyan
Yerevan Physics Institute, Yerevan, Armenia

Abstract

We propose to determine the gluon spin density within the nucleon by measuring the asymmetry of polarized photoproduction of charmed quarks from a polarized target. The experiment will be in End Station A at SLAC, using a large solid angle muon spectrometer. Photoproduction of open charm will be tagged by decays of D mesons into high transverse momentum muons. The parallel/anti-parallel asymmetry for producing open charm is closely related to the fundamental polarized gluon spin density $\Delta g(x)$. The asymmetry for single muons will be measured as a function of muon momentum, muon transverse momentum, and photon beam energies with sufficient precision to discriminate among models of $\Delta g(x)$ that differ from each other by as little as 10% in the range $0.1 < x < 0.5$. Significant constraints will be placed on both the shape and magnitude of $\Delta g(x)$ in this x region. The projected errors are significantly smaller than for other experiments that plan to make direct measurements of $\Delta g(x)$. The photon beam will be quasi-mono-chromatic and circularly polarized. It will be produced by polarized electrons hitting an oriented diamond crystal. The target will be longitudinally polarized LiD at a temperature of 300 mK, centered in a 6.5 T magnetic field to obtain a polarization of 60%. We request two months of data taking at 120 Hz (assuming joint running with PEP-II), and two weeks of checkout time to carry out this proposal.

Contents

1 Introduction

The spin degree of freedom has, in recent years, opened up a new window into our understanding of nucleon structure and electroweak interactions within the Standard Model. Much of this improvement is due to the availability of the high energy, high current, and high polarization SLAC electron beam. The fixed target program has, in addition, taken advantage of recent major advances in polarized target technology to make the world's most precise measurements [1, 2, 3, 4, 5, 6] of the proton and neutron longitudinal spin structure function g_1. One of the goals of these experiments has been the determination of the spin distributions of the quarks and gluons using the evolution equations [7]. We propose to continue this program by directly measuring the gluon spin distribution function. Another goal has been to test QCD through comparisons of data and theory for the integral difference $\Gamma_{BJ} = \int_0^1 [g_1^p(x) - g_1^n(x)]dx$. The theoretical prediction for Γ_{BJ} [8] (known as the Bjorken Sum Rule) is fundamental in QCD, and is quite sensitive to the strong coupling constant α_s evaluated at a scale of order a few GeV.

1.1 Spin Distribution Functions from g_1

A major goal of the g_1 experiments has been the determination of spin distributions of quarks and gluons in the nucleon ("what carries the spin?"). A "spin crisis", resulting in numerous theoretical papers, arose when early determinations [9] of $\Delta\Sigma = \Delta u + \Delta d + \Delta s$ were found to be much smaller than expected [where $\Delta f = \int_0^1 \Delta f(x, Q^2)dx$, and $\Delta f(x, Q^2)$ are the individual polarized quark spin distribution functions]. At present, the world average for $\Delta\Sigma$ is approximately 0.23 ± 0.07 [10], much smaller than the relativistic quark model prediction of 0.58 [11]. One explanation for at least part of this discrepancy is that the strange sea may be highly polarized, but this depends rather strongly on assumptions of SU(3) symmetry between the beta decays in the baryon octet. In any case, the low value of $\Delta\Sigma$ implies strong gluon contributions via loop and radiative corrections in QCD, expected to be stronger in the polarized case than in the unpolarized case due to the triangle diagram axial anomaly [12].

Many authors have made fits to the existing data on g_1 to parameterize the spin distribution function (SDF's) $\Delta u(x)$, $\Delta d(x)$, $\Delta s(x)$, and $\Delta g(x)$. The functions are fit at a reference scale Q_0, and evolved in Q^2 according to the GLAP equations [7]. The full NLO evolution equation splitting functions and Wilson coefficients for the polarized case have been evaluated [13]. Due to the imprecision of present data, several constraints are placed on the x-dependence (based, for example, on constituent counting rules [17]), and on overall magnitudes (i.e. the Bjorken Sum Rule must be satisfied) in order to reduce the number of free parameters. The result is that the gluon distributions found by various authors differ quite significantly, as can be seen in Figs. 1 and 2 at $Q^2 = 4$, and Fig. 3 at $Q^2 = 10$. Some older fits showing $\Delta g(x)$ are in Fig. 4a where the models used are from Ref. [17] (solid curve, $\Delta G = \int_0^1 dx \Delta g(x) = 0.7$), Ref. [18] (dashed curve, $\Delta G = 1.7$), Ref. [19] (dotted curve, $\Delta G = 2.3$), Ref. [20] (AR model, dash-dot curve, $\Delta G = 1.1$), and Ref. [20] (OS model, short dash curve, $\Delta G = 1.0$). In Fig. 4b, the five models have been divided

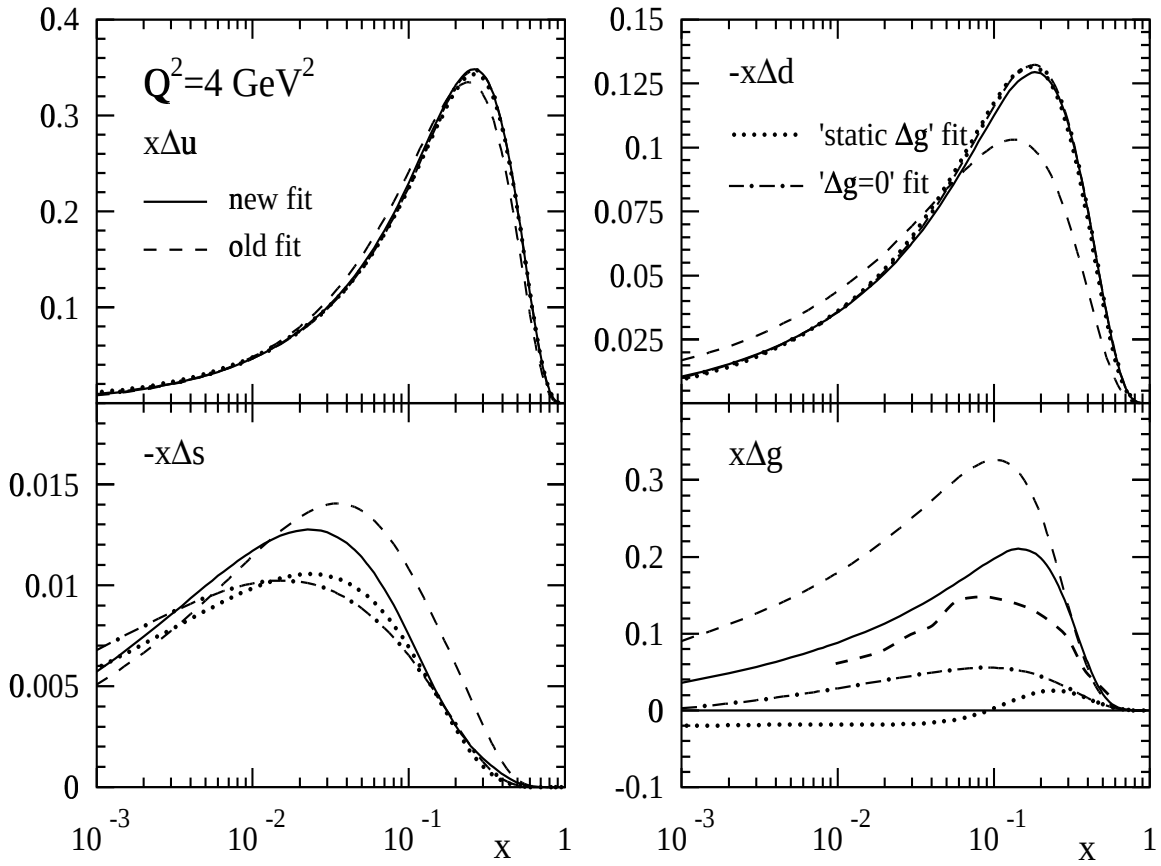

Figure 1: The polarized gluon density $x\Delta g(x)$ as calculated by GRSV [14]. Also shown is the result of the SMC fit [15] as the lower dashed line.

by a common model for $g(x)$ [17] to display the differences in the mid-x region. The fits have been done at a variety of Q_0^2 scales (from 1 to 10 GeV^2), and using different factorization schemes. Bringing all the models to a common value of Q^2 (such as the charmed mass squared, about 10 GeV^2) and a common factorization scheme (such as $M\bar{S}$) would introduce corrections that are generally smaller than the differences between the models themselves, illustrating that the present data on g_1 allow for a very broad range of fits. Some of the newer fits also have maximum values of $\Delta g(x)/g(x)$ close to unity. There is a large variation in the x distributions for $x\Delta g(x)$ and a corresponding large range in values in the total spin from the gluon, ΔG, from near zero to over 2. One calculation [21] of $\Delta g(x)$ in the context of the MIT Bag Model finds the opposite sign for $\Delta g(x)$ than for the models shown. Figure 1 illustrates that the different fits are almost identical for the $\Delta u(x)$ and $\Delta d(x)$ distributions in the measured regions. According to GRSV [14], inevitably the large uncertainty in $\Delta g(x)$ implies that the small x behavior of g_1 is completely uncertain and not reliably predictable, with values ranging from less than 5 to greater than 10 at $x = 0.0001$.

Since $g(x)$ and $\Delta g(x)$ fall with x at least as fast as $(1-x)^4$, there is essentially no experimental sensitivity to either $g(x)$ or $\Delta g(x)$ for $x > 0.5$, as can be seen in Figs. 1 and

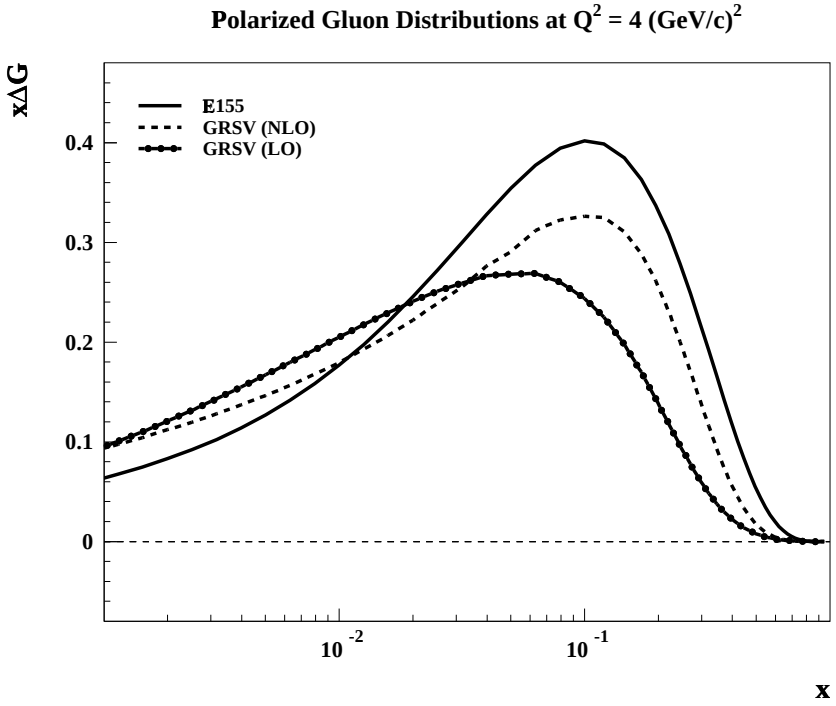

Figure 2: The polarized gluon density $x\Delta g(x)$ as calculated from a pQCD NLO fit by the E155 collaboration[6]. Also shown are the 1996 fits of GRVS[19].

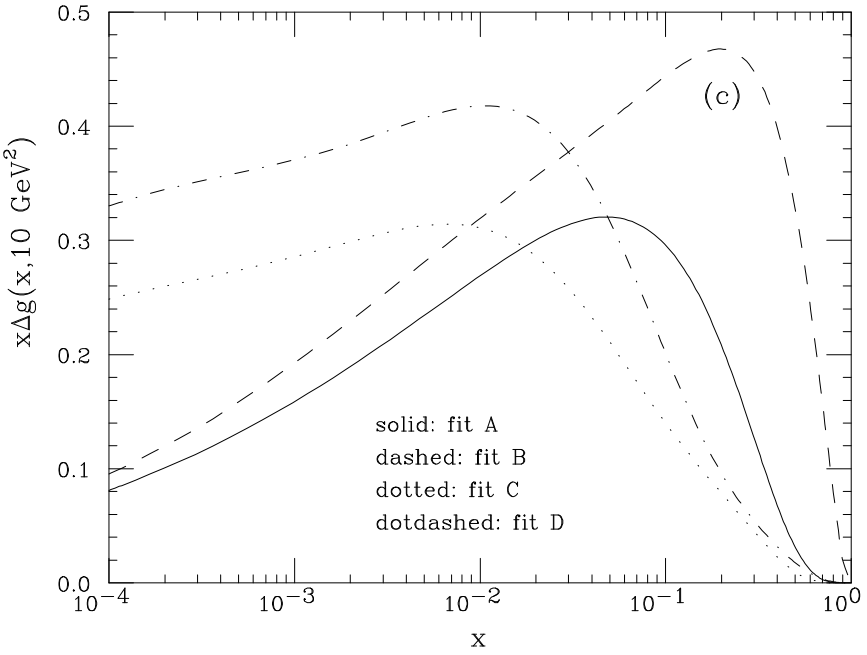

Figure 3: The polarized gluon density $x\Delta g(x)$ as calculated by Altarelli, Ball, Forte and Ridolfi[16] in 1998 for four different parameterizations.

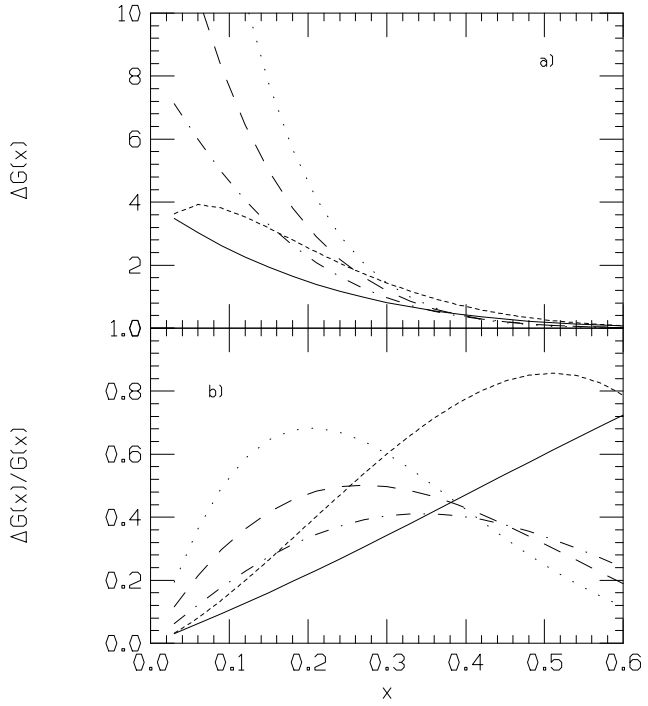

Figure 4: The polarized gluon density $\Delta g(x)$ for five representative models (see text): a) $\Delta g(x)$; b) $\Delta g(x)/g(x)$.

3. In the region $0.1 < x < 0.3$, present data allow $\Delta g(x)/g(x)$ to be anywhere between 0 and close to 1, and the x dependence of different models varies greatly. Additional measurements of g_1 will not significantly improve the situation because the inclusive g_1 measurements do not allow an unambiguous distinction to be made between the sea quark and gluon contributions. In addition, there could be substantial higher twist contributions to the g_1 data (expected to decrease as $1/Q^2$), which have not been included in the QCD fits because of the difficulty in calculating the x dependence of these contributions (only the first moments have been calculated [22]). With the limited range of Q^2 available in the g_1 data, it is difficult to distinguish between power law higher twist contributions and the logarithmic gluon contributions to the Q^2 dependence of g_1.

1.2 Direct Measurements of Gluon Spin Distribution Function

To determine the polarized gluon density, it is necessary to measure it using a directly sensitive process. The first such experiment (Fermilab E704 [23]) used polarized proton scattering on a fixed target and measured two jet production (from gg collisions) to rule out $\Delta g(x)/g(x)$ as large as 1 at $x \approx 0.15$, but could not distinguish between models that are between 0 to 0.6 (such as the curves in Figs. 1, 3, and 4). The measurement of $\Delta g(x)/g(x)$ from HERMES [24] at $x = 0.15$ and $Q^2 = 2$ is compatible with values between 0.0 and 0.8 at the two standard deviation level. There is some question about the interpretation of this result because of the relatively low energy and transverse momentum.

Figure 5: The photon-gluon fusion diagram.

Several methods have been proposed to further study $\Delta g(x)$. Approaches which use different beams and hard scattering process are complementary because they have different experimental and theoretical uncertainties. Comparing experiments also tests pQCD for spin dependent processes, just as we test pQCD and search for new physics in the spin averaged case by seeing if the same parton distributions describe a broad range of phenomena over very large ranges of kinematics.

An experiment at RHIC [26] plans to look for high transverse momentum photons coming from polarized proton-proton scattering. The kinematics are chosen to emphasize the process $q+g \to \gamma+q$, and accesses the region $0.05 < x < 0.33$. The statistical precision is expected to give errors on $\Delta g(x)/g(x)$ on the order of 0.01 to 0.3 over this x range. The interpretation is somewhat complicated because contributions for polarized quarks must be carefully taken into account. This program is expected to begin around May 2001.

1.2.1 Open Charm

The most promising approach for studying polarized gluons in the nucleon is photo- or electro-production of either open charm or inelastic J/ψ's through the hard process of photon-gluon fusion $\gamma + g \to c\bar{c}$ (see Fig. 5). Other mechanisms for producing charm are suppressed because of the large ($\sim$ 1.5 GeV) mass of the charm quark. Intrinsic charm contributions to the nucleon are expected to be very small at our kinematics of $x \leq 0.3$ and $k_\gamma \geq 35$ GeV [25].

Open charm production is directly interpretable in terms of the photon gluon fusion process [12, 27, 28]. Higher order diagrams have been calculated for both the polarized [29, 30] and unpolarized [31] case. The relatively large charm quark mass ensures that the

relevant momentum transfer scale μ^2 of the problem is of order $\mu^2 = 4m_c^2 \approx 9$ GeV^2, in which case $\alpha_s(\mu^2)/\pi \sim 0.08$, and perturbative QCD is expected to work reasonably well. Figure 6 shows the effect on A_{cc} (see Eq. 7) of NLO compared to LO for several different gluon distribution functions. The corrections are significant but have the same general effect on all the models of making the asymmetry more positive for our energy range of $\sqrt{s_{\gamma p}} < 10$ and preserving or enhancing the differences between models. Experimentally, the cross section ranges from 200 nb to 300 nb for photons between 35 and 48 GeV ($8.1 \leq W_{\gamma p} \leq 10$ GeV), as shown in Fig. 7.

Several proposals have already been made to measure polarized open charm production. The COMPASS [32] collaboration at CERN plans to make measurements with photons with energies between 35 and 85 GeV, and detect open charm principally through various D meson decays. They expect to start taking data in June 2001 and will ultimately achieve an error of 0.04 on the asymmetry. The HERMES experiment at DESY is equipped to measure open charm through the process $D \to K\pi$ [33] with photon energies below 27 GeV. Unfortunately their photon energy is comparatively low, resulting in potential problems with associated production and low values of the QCD scale. Their statistical precision is also severely limited. There has also been an evaluation of the possibility of using colliding polarized proton and electron beams at HERA (beyond the year 2002) to study polarized open charm production [35]. This would be primarily sensitive to $\Delta g(x)$ at very low x.

1.2.2 J/ψ

The asymmetry for J/ψ photoproduction has been calculated [27] and is proportional to a ratio of convolution integrals over $\Delta g(x)$ and $g(x)$. Unpolarized J/ψ electroproduction has been used by the EMC and NMC experiments to measure $g(x)$ [34], with kinematic cuts of $z < 0.9$ and $p_T^2 > 1$ GeV^2 to suppress strong contributions from Pomeron exchange. Determining $g(x)$ requires a large normalization factor K that takes into account higher order processes in the J/ψ formation from the $c\bar{c}$ pair. Unfortunately the theoretical situation for polarized production is less certain due to gluon emission which can be of low momentum, but still carries spin 1.

1.3 Overview

We expect to make a determination of $\Delta g/g$ with a statistical precision of about a factor of 10 better than other experiments using photon-gluon fusion, and in addition test the reaction mechanism and probe the x-dependence of $\Delta g(x)$ by making measurements in many kinematic bins.

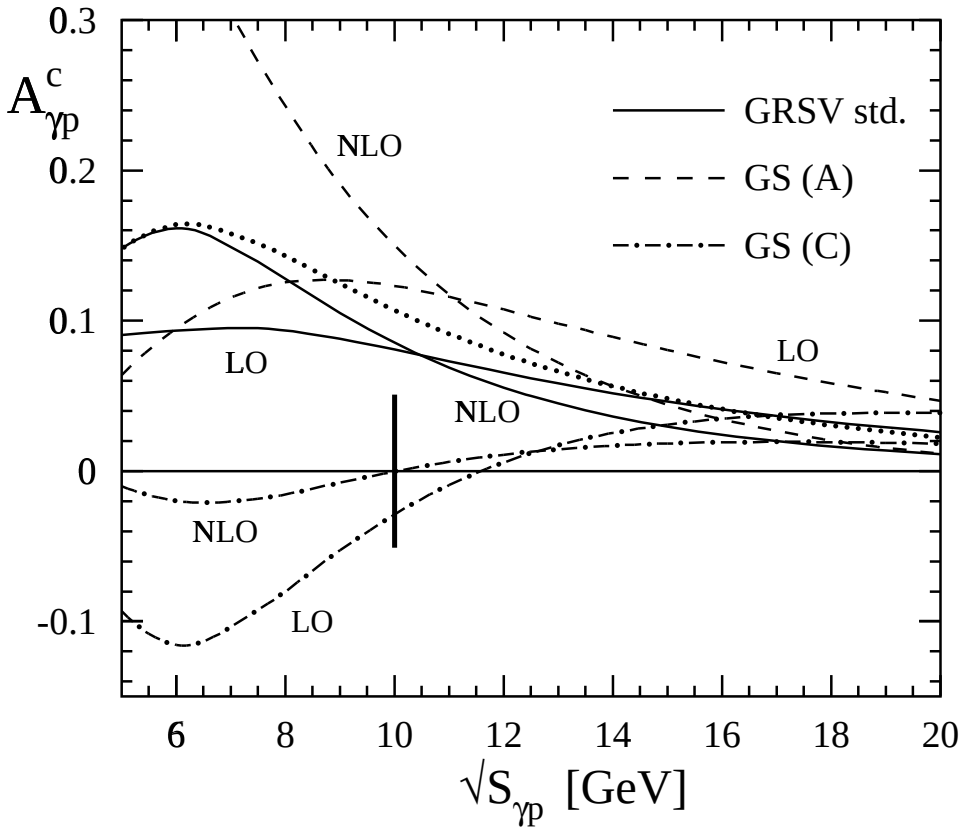

Figure 6: The effects of NLO compared to LO pQCD calculations of $A^c_{\gamma p}$ (A_{cc} in text) for several different models of the gluon polarization. The dotted curve uses the GRSV NLO gluons for the LO asymmetries. The figure is taken from [29].

Figure 7: Compilation of world data on the total open charm photoproduction cross section. The model used for the W range of this proposal (8.1 to 9.5 GeV, corresponding to photon energies of 35 to 48 GeV), is shown as the solid curve.

2 Polarized Open Charm Photoproduction

2.1 Introduction

The principal goal of the present proposal is to use polarized open charm photoproduction, tagged by the decays of D mesons into high transverse momentum prompt muons, to learn about $\Delta g(x)$ in the region $x > 0.1$. We first discuss the photon gluon fusion process, which is expected to be the dominant diagram for open charm production. We then explore how the experimental asymmetry in the counting rates for left- and right-handed circularly polarized photons impinging on a longitudinally polarized nucleon target can be related to $\Delta g/g$. Details of how open charm can be tagged using prompt muons are discussed, and reasons given why this method is the best one to use at SLAC, where a high intensity photon beam is available, but with a poor duty cycle. The next subsections deal with the backgrounds, and this section concludes with a comparison of expected error bars with calculations of the asymmetry made with a variety of models of $\Delta g(x)$.

2.2 The Photon Gluon Fusion Diagram

The dominant mechanism for production of heavy quarks from photon-nucleon interactions is the photon-gluon fusion diagram shown in Fig. 5. The spin-averaged experimental cross section is given by an integral over the product of the elementary photon-gluon cross section $\sigma(\hat{s}, \cos(\theta^*))$ with the gluon distribution $g(x, Q^2)$ [36] and the experimental efficiency $\epsilon(\hat{s}, \cos(\theta^*))$

$$\sigma_{\gamma p}(k) = \int_{x_{min}}^{1} g(x, Q^2) dx \int_{-1}^{1} \sigma(\hat{s}, \cos(\theta^*))\ \epsilon(\hat{s}, \cos(\theta^*))\ \beta\ d\cos(\theta^*) \tag{1}$$

where k is the photon energy, $x_{min} = 4m_c^2/2Mk$, m_c is the charmed quark mass of about 1.5 GeV, M is the nucleon mass, $s = 2Mk + M^2$ is the square of the c.m. energy in the photon-nucleon system, $\beta = \sqrt{1 - 4m_c^2/\hat{s}}$ is the c.m. velocity of the charmed quark, $\hat{s} = xs$ is the square of the c.m. energy in the photon-gluon system (or the $c\bar{c}$ system), Q^2 is the squared momentum transfer to the gluon (taken in our calculations to be $Q^2 = \hat{s}$), θ^* is the c.m. angle of the charmed quarks, and

$$\sigma(\hat{s}, \cos(\theta^*)) = \frac{4}{9} \frac{2\pi\alpha\alpha_s(\hat{s})}{\hat{s}} \left[\frac{-8m_c^4\hat{s}^2}{\hat{t}^2\hat{u}^2} + 2\frac{\hat{t}^2 + \hat{u}^2 + 4m_c^2\hat{s}}{\hat{t}\hat{u}} \right] \tag{2}$$

where $\hat{t} = \frac{\hat{s}}{2}[1 + \beta\cos(\theta^*)]$, and $\hat{u} = \frac{\hat{s}}{2}[1 - \beta\cos(\theta^*)]$. For small β ($\hat{s} < 15$ GeV^2), $\sigma(\hat{s}, \cos(\theta^*))$ is approximately independent of $\cos(\theta^*)$, and the integrated form

$$\sigma(\hat{s}) = \frac{4}{9} \frac{2\pi\alpha\alpha_s(\hat{s})}{\hat{s}} \left[-\beta(2 - \beta^2) + \frac{1}{2}(3 - \beta^4) \ln\frac{1 + \beta}{1 - \beta} \right]. \tag{3}$$

can be used.

The charmed quarks undergo the fragmentation process once they are produced, with the result that, on average, a little less than two D mesons are produced per $c\bar{c}$ pair. Occasionally, Λ_c and η_c are observed in the final state as well (see Table 1).

	D^+	D^0	D_s^+	Λ_c^+
produced	0.19	0.63	0.08	0.08
decay to μ^+	0.37	0.47	0.08	0.04
	D^-	$\bar{D}^0$	D_s^-	Λ_c^-
produced	0.21	0.71	0.06	0.02
decay to μ^-	0.40	0.53	0.05	0.01

Table 1: Fraction of different charmed particles produced with k=40 GeV photons and a deuterium target with $p_T > 0.5$ GeV using open charm events generated using PYTHIA 5.7 [39]. Also shown is the fraction of muons of each charge which originate from the parent charmed particle. Almost all the muons come from D mesons because of their larger production cross section and larger branching ratio to muons. HERWIG gives similar results.

The total cross section for this process has been fairly well measured [37] and averages about 170 nb for photons between 39 and 48.5 GeV. The transverse momentum (p_T) dependence of the D mesons is exponential and falls as $d\sigma/dp_T^2 \approx e^{-p_T^2/<p_T^2>}$, with a mean value of $< p_T^2 > \approx 1$ GeV^2. The distribution in x_F is approximately Gaussian with a mean value of 0.2 and a width of 0.5. NLO corrections have been calculated, and change the total cross section by about 35%, but have little effect on the p_T and x_F distributions. The magnitude of the cross section, the x_F dependence, and the p_T dependence are in very good agreement with predictions from the photon-gluon fusion process, using gluon distributions determined from other reactions [37].

For polarized photons and longitudinally polarized nucleons, the polarized experimental cross section component $\Delta\sigma_{\gamma p}(k)$ is given by [27]

$$\Delta\sigma_{\gamma p}(k) = \int_{x_{min}}^{1} \Delta g(x,Q^2)dx \int_{-1}^{1} \Delta\sigma(\hat{s},\cos(\theta^*))\ \epsilon(\hat{s},\cos(\theta^*))\ \beta\ d\cos(\theta^*) \tag{4}$$

where

$$\Delta\sigma(\hat{s},\cos(\theta^*)) = \frac{4}{9}\frac{2\pi\alpha\alpha_s(\hat{s})}{\hat{s}}\Big[\frac{4m_c^4(\hat{t}^3+\hat{u}^3)}{\hat{t}^2\hat{u}^2} + 2\frac{\hat{t}^2+\hat{u}^2-2m_c^2\hat{s}}{\hat{t}\hat{u}}\Big]. \tag{5}$$

Integrated over $\cos(\theta^*)$, this becomes

$$\Delta\sigma(\hat{s}) = \frac{4}{9}\frac{2\pi\alpha\alpha_s(\hat{s})}{\hat{s}}\Big[-3\beta + \ln\frac{1+\beta}{1-\beta}\Big]. \tag{6}$$

This is a reasonable approximation for $\hat{s} < 15$ GeV^2, as can be seen in Fig. 8, where $\sigma(\hat{s},\cos(\theta^*))$ and $\Delta\sigma(\hat{s},\cos(\theta^*))$ are plotted versus $\cos(\theta^*)$ over the range from 0 to 1 (-1 to 0 is mirror symmetric). Although $\sigma(\hat{s},\cos(\theta^*))$ is relatively slowly varying, $\Delta\sigma(\hat{s},\cos(\theta^*))$ changes sign for $\hat{s} > 20$ and $|\cos(\theta^*)| < 0.8$, so it is important to include the experimental efficiency $\epsilon(\hat{s},\cos(\theta^*)$ when evaluating the total polarized counting rate for a given kinematic setting. The best sensitivity comes from an experimental efficiency that emphasizes mostly positive or negative $\Delta\sigma(\hat{s},\cos(\theta^*))$. On the other hand, kinematics that emphasize the transition through zero are less sensitive to $\Delta g(x)$, but test the underlying reaction mechanism.

2.3 Experimental asymmetry for open charm

For a mono-chromatic photon beam, the ratio of $\Delta\sigma_{\gamma p}(k)/\sigma_{\gamma p}(k)$ is directly proportional to the experimental asymmetry

$$A_{cc}(k) = \frac{1}{P_t P_b f}\ \frac{N^{\uparrow\uparrow} - N^{\downarrow\uparrow}}{N^{\uparrow\uparrow} + N^{\downarrow\uparrow}} = \frac{\Delta\sigma_{\gamma p}(k)}{\sigma_{\gamma p}(k)} \tag{7}$$

where P_t is the target polarization, P_b is the photon beam polarization, and f is the target dilution factor (fraction of polarizable nucleons). The rates of detected muons normalized to the incident beam flux for parallel and anti-parallel spins are denoted by $N^{\uparrow\uparrow}$ and $N^{\downarrow\uparrow}$.

By measuring the asymmetry A_{cc}, the sensitivity to common factors (such as the scale at which $\alpha_s(\mu^2)$ is evaluated, the charm quark mass, or the branching ratios for D decays

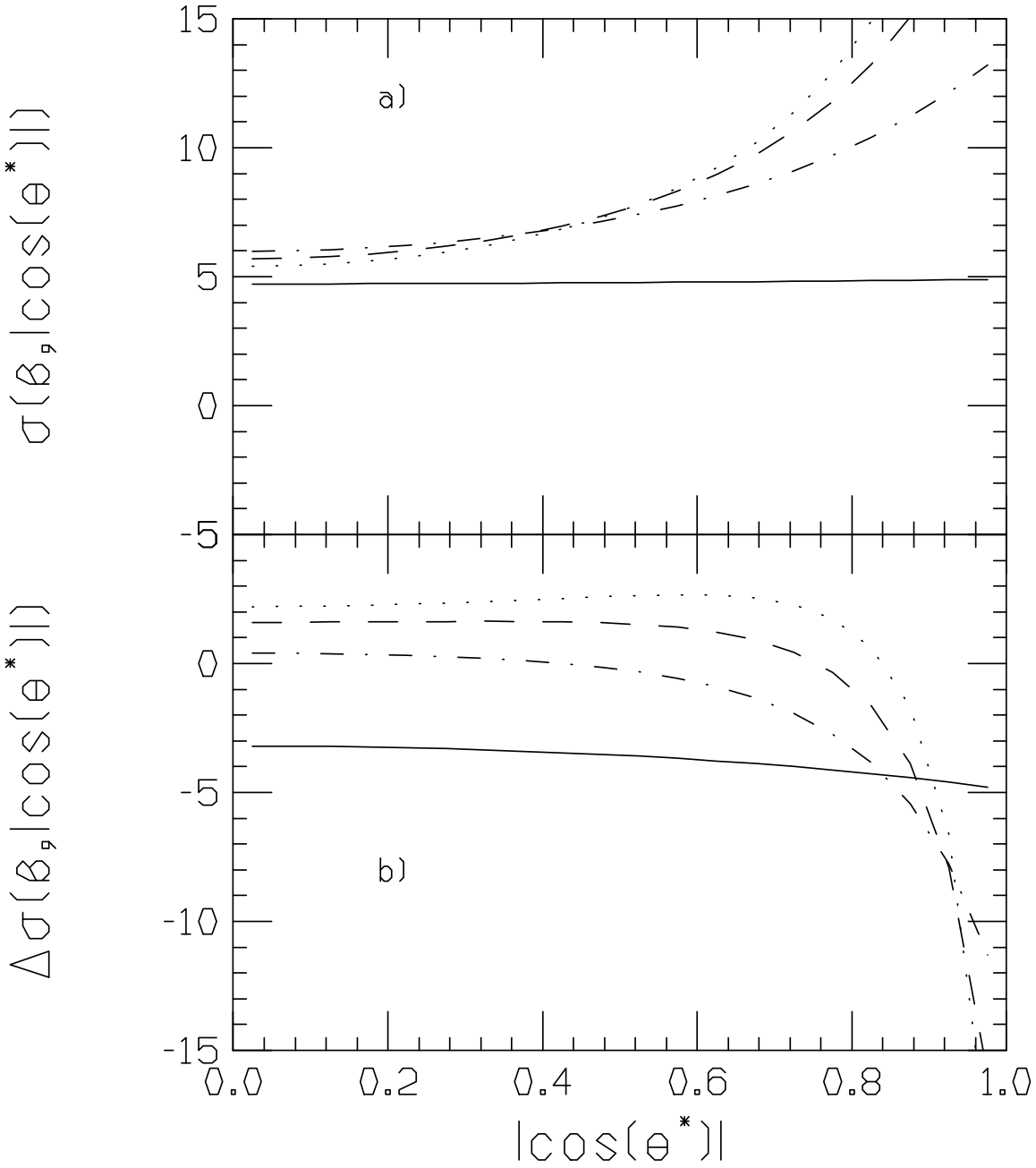

Figure 8: The a) spin-averaged and b) spin-dependent cross sections for $\gamma g \to c\bar{c}$ (scaled by $9\hat{s}/8\pi\alpha\alpha_s(\hat{s})$, and assuming $m_c = 1.5$ GeV) as a function of $\cos(\theta^*)$ for four values of $\hat{s}$: 10 (solid curve); 20 (dash-dot), 30 (dashes); and 40 GeV^2 (dots). The corresponding values of β are 0.3, 0.74, 0.84, and 0.88.

to muons) cancel out, reducing the theoretical uncertainty. Additional uncertainties remain from QCD diagrams beyond NLO. There is the possibility that polarization dependence in the fragmentation process could change the kinematics of the produced D mesons and hence of their decay muons. We minimize this effect by comparing results from both muon signs over a large range of kinematics as explained in Sec. 2.4.

For a continuous-energy-distribution photon beam (such as bremsstrahlung), the experimental asymmetry depends on the ratio of integrated predicted experimental rates:

$$A_{cc}(E) = \frac{1}{P_t P_b f} \frac{N^{\uparrow\uparrow} - N^{\downarrow\uparrow}}{N^{\uparrow\uparrow} + N^{\downarrow\uparrow}} = \frac{\int_0^E dk D(k)\Phi(k)\Delta\sigma_{\gamma p}(k)}{\int_0^E dk \Phi(k)\sigma_{\gamma p}(k)} \tag{8}$$

where the photon flux $\Phi(k) \approx \frac{(t/X_0)}{k}$ for bremsstrahlung from an amorphous material, where t is the thickness of a radiator with radiation length X_0 through which the electron beam passes, and the depolarization factor is $D(y) \approx [1-(1-y)^2]/[1+(1-y)^2]$, where $y = k/E$, and E is the photon endpoint energy (the energy of the primary electron beam). As discussed in more detail below, we plan to use bremsstrahlung from a diamond crystal, oriented to give a large enhancement of the flux at high photon energies, compared to the incoherent flux characteristic of amorphous materials.

We plan to detect D mesons by their semi-leptonic decays to muons. Since large p_T muons are strongly correlated with even higher p_T D mesons, the average $x = \hat{s}/s$ of the gluon probed increases with the p_T of the muon. This is because large p_T charmed mesons are correlated with large $\sqrt{\hat{s}}$, by conservation of momentum.

2.4 Associated Production

Ideally our experiment would measure photon-gluon fusion where the produced c and $\bar{c}$ are isolated from the target fragments and thus not affected by the polarization of the target remnants. In the limit of very high energy incoming photon, this is the case. At our energies the hadronization process includes some coupling between the charmed quarks and the target quarks. A measure of this coupling of produced charm quarks with target quarks is the difference in the production rates of Λ_c and $\bar{\Lambda}_c$. The former can be produced from a diquark from the target, while the latter cannot be. We have used HERWIG 6.1 [38] to examine the photon-gluon fusion interactions that have a final state muon from charm decay. We tested HERWIG against data from experiments both below and above our energy range. At 20 GeV HERWIG predicts a ratio of $\sigma(\Lambda_c)/\sigma(charm) \sim 0.8$ which is consistent with the experimental value from the SLAC Hybrid Facility [40] of $(71 \pm 11 \pm 6)\%$. At an average photon energy of 90 GeV, NA14/2 [41] estimated that $(\Lambda_c + \bar{\Lambda}_c)/(D + \bar{D}) \sim 0.15 \pm .06$ a little higher than the HERWIG calculation of 0.04.

We have used the Monte Carlo programs HERWIG 6.1 [38] and PYTHIA 5.7 [39] (with the parameter MSTP(92)=1, as favored by data [42]) to calculate the effects of associated production. There is rough agreement between the two Monte Carlos. We present the average results. The difference between the rate of events which have a Λ_c and $\bar{\Lambda}_c$ is used to measure the effects of the target fragments. This is shown in Fig. 9 For μ^+ the fraction $(\Lambda_c - \bar{\Lambda}_c)/(\mu)$ rises slowly from 1% at $k_\gamma = 49$ GeV to 3% at $k_\gamma = 35$ GeV. Thus at our

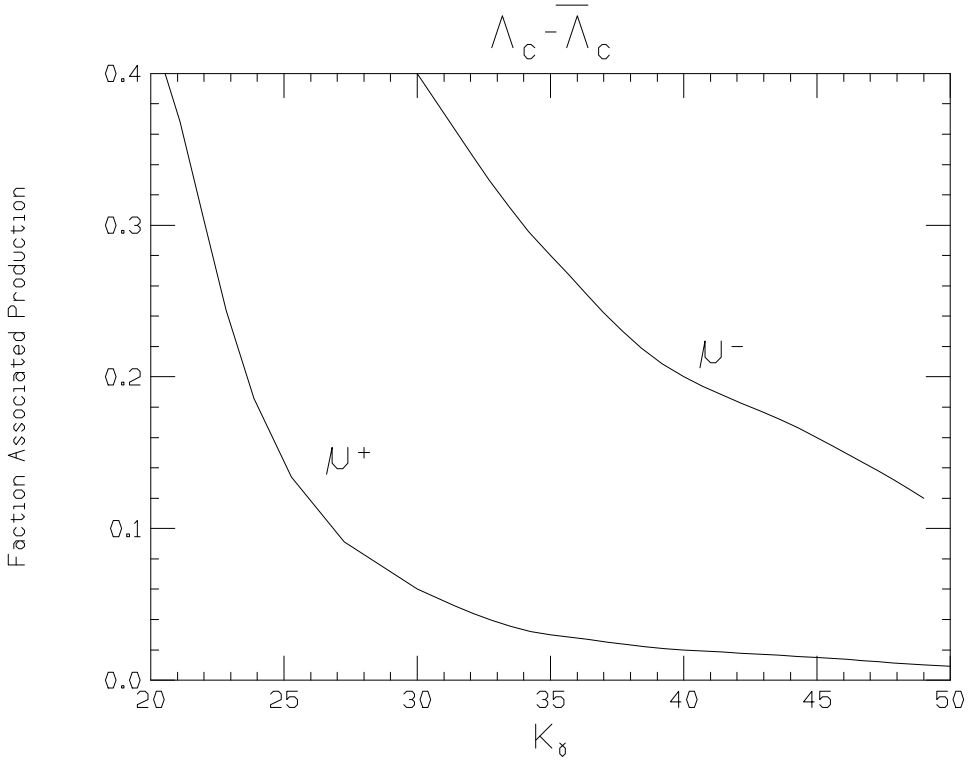

Figure 9: Fraction of open charm events with detected muon decay from associated production of $\Lambda_c + D$ vs. photon energy. This is measured from the difference between Λ_c and $\bar{\Lambda_c}$ production. The two curves correspond to detected μ^+ and μ^-. Note that for beam energies greater than about 35 GeV associated production of μ^+ is only a few percent. The results are from an average of PYTHIA and HERWIG.

energies, this associated production of Λ_c is small for μ^+. For μ^-, the effect is much larger, rising from 12%, to 28% over the same energy range. This is because μ^- predominantly comes from $\bar{c}$ via D^- and $\bar{D^o}$ with the possibility of the c combining with the target fragments. The μ^+ comes predominantly from c via D^+ and D^o leaving a $\bar{c}$ which is unable to combine with a target diquark. Below 30 GeV incident energy associated production rises rapidly, increasing the difficulty of theoretical interpretation.

Another measure of the coupling between the charmed quarks and the target quarks is the number of clusters (in HERWIG) of particles produced. The more clusters, the larger separation between the decaying $\bar{c}$ and any possible effects from hadronization to Λ_c. The probability for 2 clusters for either μ^+ or μ^- is less than 1% at 49 GeV increasing to only 3% at 35 GeV, indicating that even when Λ_c is produced it is not strongly coupled to the μ^- from D^- and D^o decay.

Experimentally, any difference in asymmetries measured using μ^+ and μ^- could be attributed to target fragment interactions. Using the asymmetries measured for both μ^+ and μ^-, both the hard process photon-gluon fusion and the effects of hadronization can be separated. These μ^+ and μ^- data points with different associated production backgrounds

can be extrapolated to zero background. Because the μ^+ signal is more than 95% hard process, and the μ^- has more than 5 times the background as the μ^+, we anticipate the correction will be small and the statistical error degraded by less than 30%.

2.5 Tagging Open Charm with Single Muons

About 24% of all open charm events have at least one prompt muon in the final state. These come about equally from charged and neutral D's, since charged D's are twice as likely to decay to muons, but are only produced about half as often, with the next biggest source being D_s and Λ_c. Table 1 shows for a 40 GeV beam, the fraction of each type of parent particle from which a muon with $p_T > 0.5$ GeV and momentum $P_\mu > 3$ GeV originated. In addition there are background μ from π, K and τ decay described in the section 2.7 which are not shown in the table.

The average muon momentum from open charm events is about 3 GeV, and the average p_T is about 0.4 GeV, extending with significant counting rate to as high as 2 GeV. Fig. 10 shows (full circles) the number of muons expected from open charm as a function of p_T, for muons with momenta between 5 and 10 GeV (lower row) and between 10 and 15 GeV (upper row), for the three beam energies at which we plan to take data (from left to right, coherent peaks at 35, 40, and 45 GeV). The details of the coherent bremsstrahlung spectra at each energy are given below. We have folded each photon spectrum with the expected cross section, spectrometer efficiency, and luminosity, integrated over 6×10^7 beam spills (six days at full beam delivery efficiency). The number of counts in each p_T bin of width 0.1 GeV have been convoluted with the expected spectrometer resolution (see below). For this luminosity, the number of tagged open charm events increases from about 50,000 at very high transverse momentum, to several million events at $p_T = 0.5$ and lower muon momentum. The open charm rates flatten out at lower p_T, while the backgrounds become very large (see next section). The rates are significantly higher for the $5 < P_\mu < 10$ GeV range than for the higher $10 < P_\mu < 15$ GeV range. The open charm rates are rather similar for the three average photon energy settings because the lower cross section at the lower photon energies is compensated for by an increased coherent peak height.

The kinematic selectivity of the muons for probing photon-gluon fusion is illustrated in Fig. 11. The distribution in $x = \hat{s}/s$ versus $|\cos(\theta^*)|$ for all open charm muons produced with the 48.3 GeV endpoint beam energy is shown in Fig. 11a. It is rather similar to the distribution for $5 < P_\mu < 10$ and $0.6 < p_T < 0.7$ (see Fig. 11b), a kinematic bin that yields a relatively small error on A_{cc}. In both cases, the average x is about 0.15. On the other hand, the events in Fig. 11c for $p_T > 1.0$ come from smaller values of $|\cos(\theta^*)|$, but larger values of x than the average $c\bar{c}$ event, and so preferentially select the region where $\Delta\sigma(\hat{s}, \cos(\theta^*))$ is small and changing sign as seen in Fig. 8. Fig. 11d shows the distribution for lower p_T muons ($0.6 < p_T < 0.7$) that have high momentum ($15 < P_\mu < 20$ GeV). In this case there is a strong selection towards large values of $|\cos(\theta^*)|$, which means the average value of $\Delta\sigma(\hat{s}, \cos(\theta^*))$ will be more negative than for lower momentum muons with the same transverse momentum (Fig. 8).

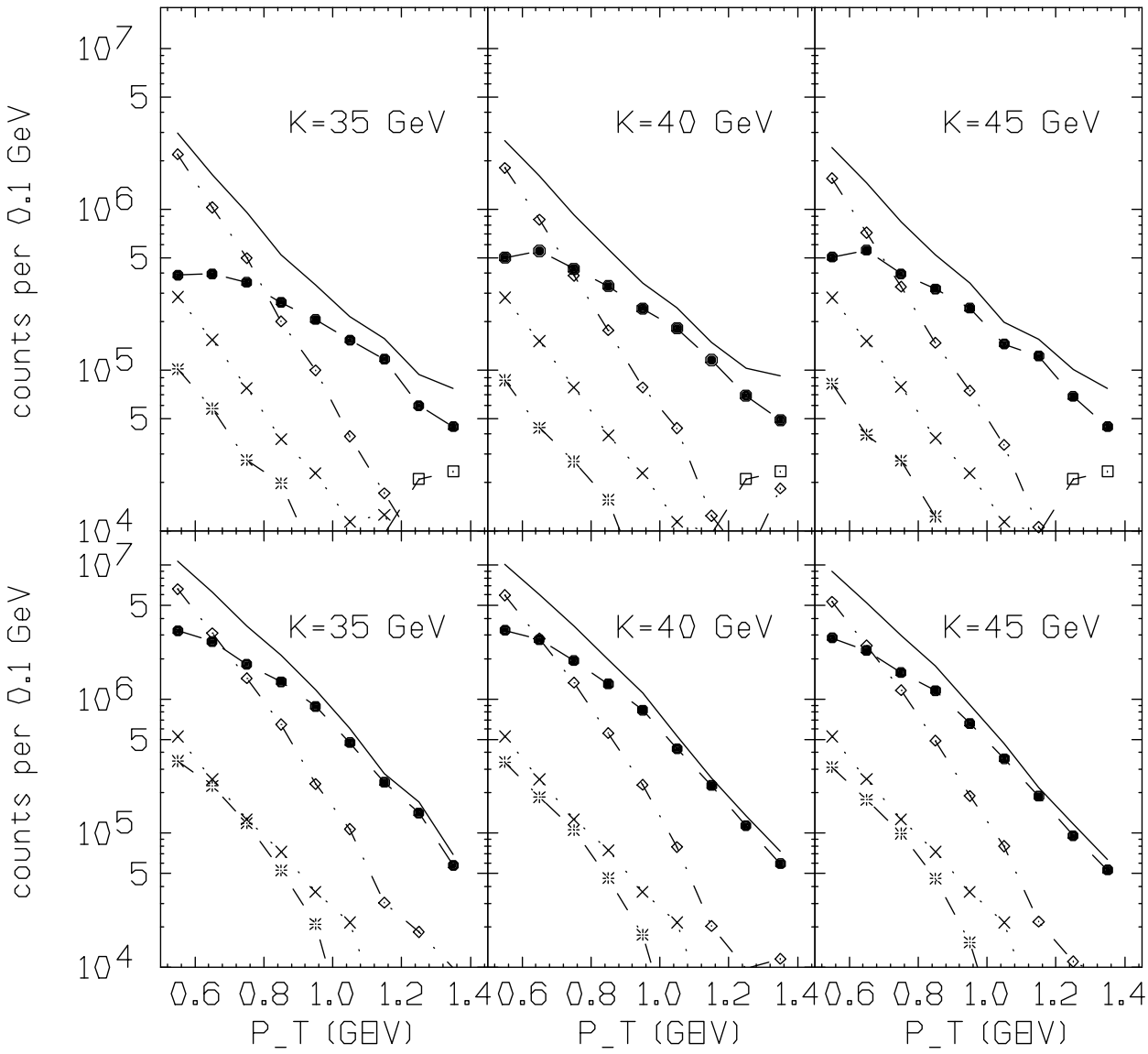

Figure 10: Number of expected counts per 0.1 GeV bin in p_T as a function of p_T for single muon events, for the three proposed beam energies (from left to right,coherent peaks at 35, 40, and 45 GeV). The top row is for muons with $10 < P_\mu < 15$ GeV, while the bottom row is for $5 < P_\mu < 10$. The solid curve is the total number of counts. The open charm counts (the experimental signal) are shown as full circles (dashed curve), the decays from pions and kaons are shown as diamonds (dash-dot curve), Bethe-Heitler counts are the crosses (dotted curve), J/ψ decays are shown as boxes (dashed curve), and decays of η, ρ, ω, and ϕ are shown as the stars (dash-dot curve).

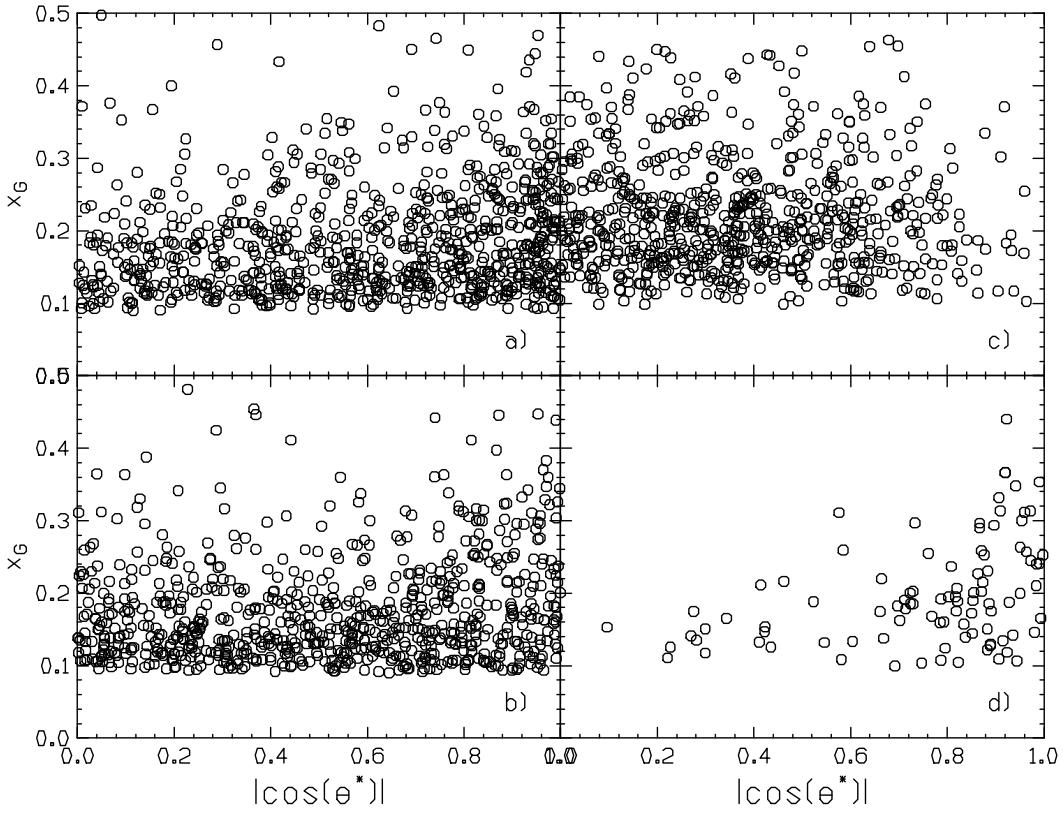

Figure 11: Distribution in $x = \hat{s}/s$ and $\cos(\theta^*)$ for: a) all open charm events; b) detected events with $5 < P_\mu < 10$ and $0.6 < p_T < 0.7$; c) $5 < P_\mu < 10$ and $p_T > 1.0$; d) $15 < P_\mu < 20$ and $0.6 < p_T < 0.7$.

2.6 Other Open Charm Tags

We have made a detailed study of alternative methods of tagging open charm that turn out to be not suited for use with the low duty cycle at SLAC. One is by the two- or three-body decay of D into pions and kaons. The best signal comes from $D^* \to \pi D^0 \to \pi K$, which gives a double kinematic constraint (the masses of the D^0 and D^*) which eliminates most combinatoric background. However, the limited duty cycle at SLAC ($< 10^{-4}$), combined with the large flux of pions and kaons that don't come from charm events limits the usable luminosity to about three orders of magnitude less than if muons are used to tag open charm. The result is that it would take much more running time to get the same error bar on A_{cc}, and the detector apparatus would be much more complicated.

We also investigated using muon pairs (one from each charmed quark) to tag open charm. The signal is greatly reduced after placing cuts needed to eliminate backgrounds, so the asymmetry errors are about five times larger than using single muons. Since the detector we propose is designed to have good efficiency over a large solid angle, it will register the two muon signal in any case, and it will provide a systematic check on the single muon results with larger statistical error..

2.7 Backgrounds

Although the open charm cross section is only about 0.2% of the total photoproduction cross section at 50 GeV, processes other than open charm rarely generate prompt muons, making the signal of one or more high transverse momentum muons a good signature for open charm. This allows us to take advantage of the high luminosity available at SLAC.

2.7.1 Pion and Kaon Decays

There are several sources of backgrounds that can generate single muons. The largest is the decay of pions and kaons. We propose to minimize this contribution by placing a copper/alumina absorber as close as possible to the target. We have calculated the flux of muons from pion and kaon decays using the approximations (checked using GEANT) that on average, muon decays occur in the first absorption length (18 cm of Cu), and that the target to absorber distance is $[5 + 0.5/\sin(\theta)]$ cm. The results are represented by the diamond symbols in Fig. 10. We have done the hadron flux calculations two ways, and they are in reasonably good agreement (within 30% of each other). The first method was to use PYTHIA, with all photoproduction processes turned on, to generate pions and kaons and keep those that decay in the canonical distance. An average was taken over proton and neutron targets, and the result scaled by 0.9 to account for nuclear shadowing in the predominant lithium component of the target (assuming inclusive photoproduction at moderate p_T scales as $A^{0.9}$). The second method was to use the parameterization of inclusive pion and kaon photoproduction of Wiser [43], which is fit to data at endpoint energies of 5 to 19 GeV. The extrapolation of the Wiser fit to 48.5 GeV is very close to the PYTHIA rates for π^+, π^-, K^-, but is about a factor of two higher for K^+, approximately independent of p_T. The rates in Fig. 10 are for the sum of μ^- and μ^+: if only μ^- is considered, the ratio of open charm signal to decay background is typically 30% larger than if only μ^+ are considered.

As a check on our calculations, we have compared the Wiser and PYTHIA predictions for inclusive negative hadrons to the cross sections measured in inclusive electroproduction from a glass/helium target in SLAC experiment E154. The calculations assume that electroproduction at an endpoint energy of 48.5 GeV is equivalent to photoproduction using a 3.5% radiator, and we make a shadowing correction of $\sim 50\%$ to the nucleons in the glass portion of the target. As can be seen in Fig. 12, the calculations match the p_T dependence of the data extremely well at the two angles measured, and the magnitude is within 20% of the data.

As seen in Fig. 10, muons from pion and kaon decays are the largest source of background. We plan to measure the relative prompt and decay muon rates by varying the distance of the absorber from the target as was done in a SLAC experiment in 1975 [44]. In the 1975 SLAC experiment, this technique was used to measure the prompt rate of muons with $P_\mu = 6$ GeV and $p_T = 1$ GeV at photon endpoint energies of 8, 12, and 20 GeV. The decay rates were found to be in good agreement with a prediction based on the Wiser fit. After correcting for the expected Bethe-Heitler prompt signal, no excess was seen at endpoint energies of 8 and 12 GeV (which are below the $D\bar{D}$ threshold), but a substantial

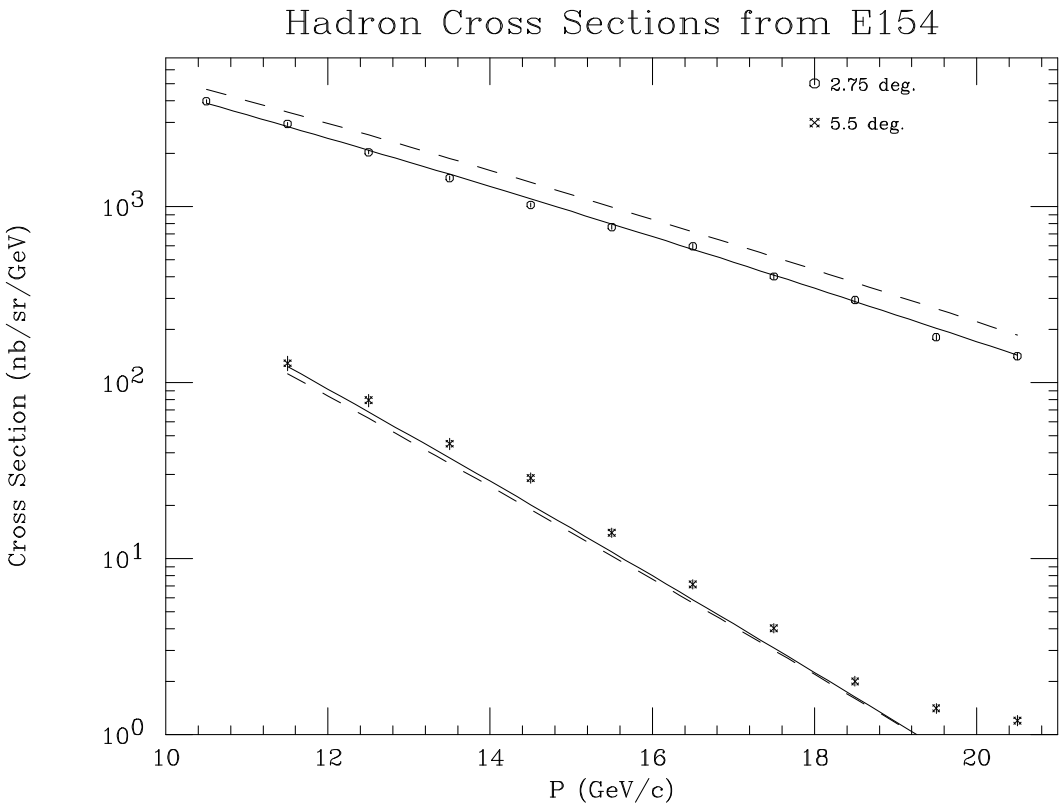

Figure 12: Inclusive electroproduction cross sections for negative hadrons measured in SLAC E154 from a glass/helium target with a beam energy of 48.5 GeV at 2.75 and 5.5 degrees. The solid lines are the predictions from the Wiser fit, while the dashed lines are from PYTHIA.

excess was seen at 20 GeV, consistent with that expected from open charm. By measuring both rates and asymmetries at two decay distances (one small and one five to ten times larger), we can determine the relative cross sections of prompt and decay muons, as well as their asymmetries. The decay length of both charged pions and kaons is an order of magnitude larger than the distances involved and are nearly equal at the same momentum. Thus the number of decay muons depends linearly on the position of the absorber. Some corrections will be needed from models of the hadron shower. We can then calculate the dilution factor α to our signal and get the asymmetry due to the open charm production using:

$$A_{cc} = \frac{1}{\alpha}[A_{\text{measured}} - (1-\alpha)A_{\pi-K}], \tag{9}$$

where $A_{\pi-K}$ is the asymmetry of the decay muons from pions and kaons discussed below. The hadron asymmetries for inclusive hadron photoproduction from deuterium measured in SLAC E155 [45], shown in Fig. 13, are very small and consistent with zero for $k_{had} \leq 15$ GeV corresponding to $p_T \leq 1.4$ (our kinematic range). The theoretical calculation of Afanasev, Carlson, and Wahlquist [46] is consistant with data and barely distinguishable from zero in this kinematic range. Other calculations [47, 48] give hadron asymmetries of

about 0.02 from a deuteron target at 40 GeV. Other hadron asymmetries from Reference [45] down to $P_t = 0.5$ are also very small and consistant with zero. Thus we expect the background asymmetries from hadron decay muons to be very small.

2.7.2 Bethe-Heitler Muon Pair Production

The second class of backgrounds is Bethe-Heitler (BH) muon pair production, in which a photon splits into a muon pair, and one of the muons scatters either a) elastically from a nucleus; b) quasi-elastically from a nucleon; or c) inelastically from a quark. The cross section for BH production is exactly calculable using the formulas of Tsai [49] as long as the form factors F_1 and F_2 are known for each of a), b), and c). From our work in calculating radiative corrections to deep inelastic electron scattering, we have good models for these form factors, and believe the resulting cross section calculations are good to better than 10%. To generate BH events with the proper weighting, we modified a Monte Carlo code (which embodies Tsai's formulas) developed at Fermilab [50], to include process c), and checked the results against the tables shown in Tsai's article. To reduce the BH background, we plan to veto events in which a second, opposite sign, muon is detected (since BH muons are always created in opposite sign pairs). For the planned detector acceptance, this removes typically 90% of the events. The true charm signal is only reduced by a few percent, since the vast majority of charm events result in only a single detected muon. An additional 2% of the charm signal is removed by a random time coincidence with a second, unrelated muon. The results are shown in Fig. 10, where it can be seen that in most cases BH/charm is less than 0.1. We can correct for the un-vetoed BH events using the Tsai formulas for the rates, and recently calculated formulas [60] for the asymmetries, which depend on the now fairly well measured spin-dependent structure functions g_1 and g_2 .

We calculated the BH rate for τ lepton pairs, which are produced at large p_T due to their heavy mass of 1.8 GeV. Taking into account the 17% probability for a τ to decay to a muon, we find the background from this source to be less than 1% of the open charm signal.

2.7.3 Decays of Light Vector Mesons

We have also considered prompt background from the decays of η, $\rho(770)$, $\omega(782)$, and ϕ mesons, as generated by PYTHIA. The branching rations are small (3.1×10^{-4}, 4.6×10^{-5}, 9.6×10^{-5}, and 2.5×10^{-4}, respectively). However, the particles are copiously produced by the soft (low p_T) Vector Dominance mechanism, in which a photon fluctuates into a vector meson and scatters hadronically from a nucleon. Because this is a low p_T process, and because the muons typically acquire an additional p_T of less than half the parent mass, the distribution of muons from vector meson decays falls much more rapidly with p_T than the open charm signal, and will result in a very small correction to the measured asymmetries.

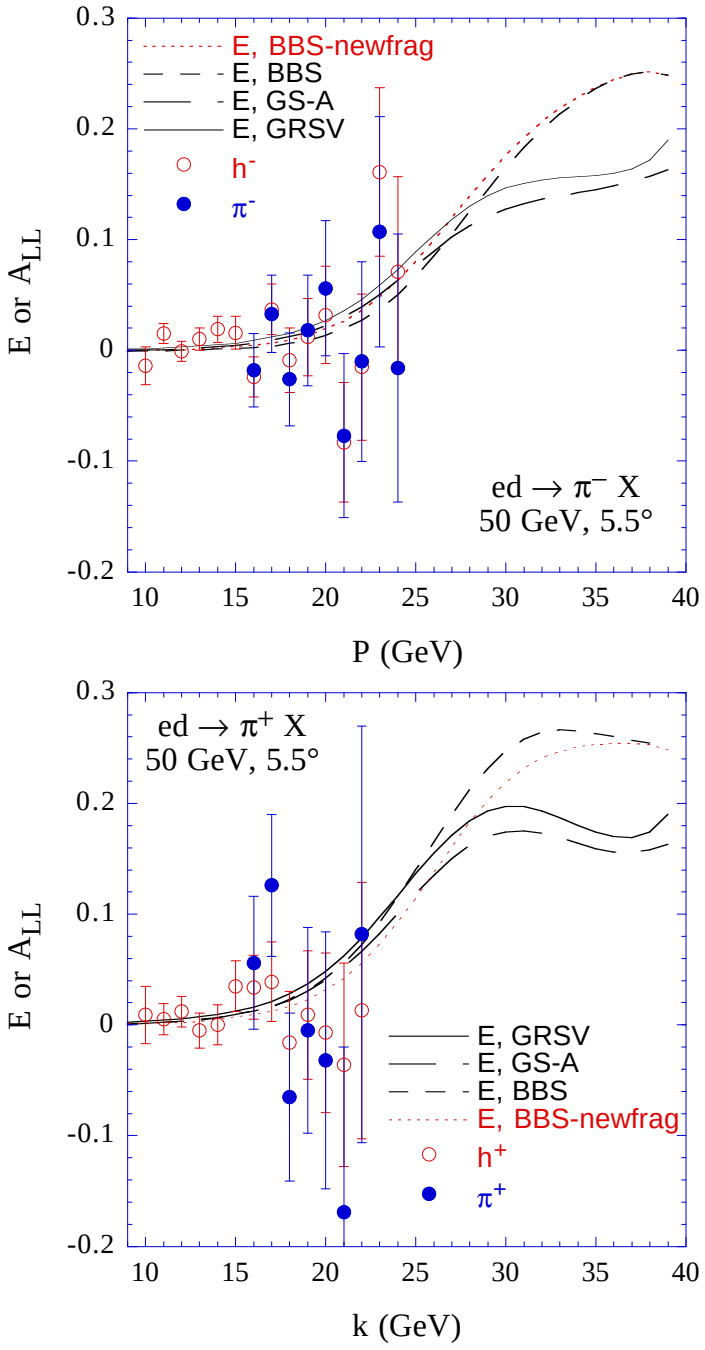

Figure 13: The helicity-dependent asymmetries $A_{||}$ for polarized photoproduction of inclusive hadrons (open circles) and pions (solid circles) from a longitudinally polarized deuteron, at 5.5^o and for both positive (+) and negative (-) particles. The figure is taken from Ref. [46], the data is from [45].

2.7.4 Decays of J/ψ

The final background we have considered is muons from J/ψ's, which decay 6% of the time to two opposite sign muons with typical transverse momentum of 1.5 GeV/c. The spectrometer acceptance is adequate to veto about 50% of the J/ψ decays; those that remain contribute a significant background for $p_T > 1.2$ GeV, although the rate is still well below the open charm rate (see Fig. 10). We will correct for the rate and asymmetry of this background using the events for which both decay muons are detected.

3 Photon Beam

3.1 Introduction

We propose to use coherent bremsstrahlung to generate the photon beam. Coherent bremsstrahlung is strongly favored in comparison with incoherent bremsstrahlung because it provides a better signal to noise when considering the total rate of muons impinging on our detectors. The total muon rate per beam spill in the detector is the factor limiting the luminosity, rather than the beam current, so the choice of coherent bremsstrahlung offers a significant advantage.

3.2 Electron and Photon Beams in the A-line

The use of coherent bremsstrahlung at SLAC was successfully demonstrated in experiment E78 [51], and we plan to use a very similar setup. This type of beam has also been used at Mainz[52]. A schematic layout of the photon beam line is shown in Fig. 14, and a summary of the properties of the electron and photon beams is given in Table 2. We will use the SLAC electron beam at three energies between 45 to 51 GeV and a current of 2×10^{10} electrons per 500 ns long beam pulse. The crystal axis will be rotated to place primary coherent photon spikes at 35, 40, and 45 GeV for electron beam energies of 45, 48, and 51 GeV respectively. We assume the accelerator will be operating in the SLED mode, at a nominal repetition rate of 120 Hz with the polarized source.

For most of the running, the electrons will be incident on an existing 0.07% radiation length (r.l.) thick oriented diamond crystal with a tilt angle θ_0 of a few milliradians. The diamond will be positioned using the SLAC goniometer [53], which can hold two radiators, and position either of them at well-defined angles with respect to the beam axis, in steps of 25 μrad. The precision needed for the coherent beam is approximately 400 μrad. The goniometer will be located just downstream of the Q27/Q28 quad pair at the end of the A-line, as in SLAC E78 [51].

We plan to reduce the thickness of the two existing thicker diamond crystals to 0.07% r.l., to be used as spares. This thickness gives the best tradeoff between photon flux and coherent peak width. The current and integrated luminosity are well below those used in E78 [51], so that it is unlikely that both diamonds in the goniometer will fail due to radiation damage or shock stresses.

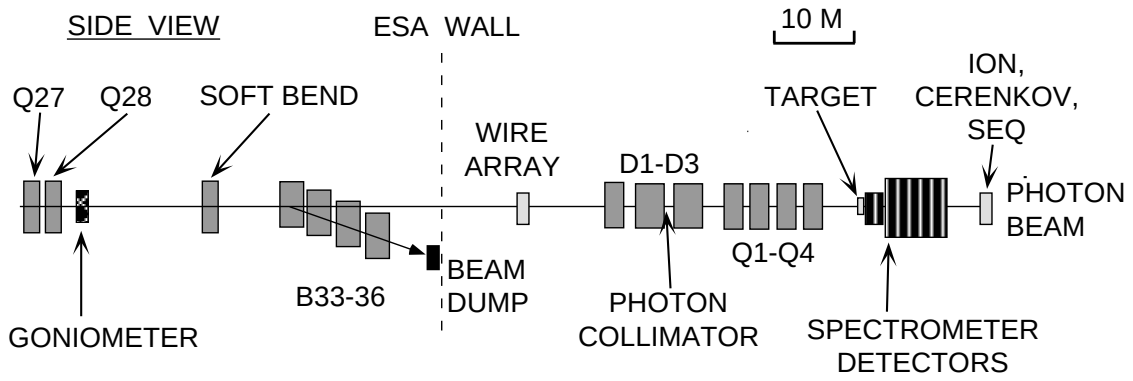

Figure 14: Overall view of the main components of the photon beam (horizontal scale is approximate, vertical scale is exaggerated). The Wire Array, D1-D3 dipole magnets, and Q1-Q4 quadrupoles are part of the current E158 setup.

The A-line quadrupoles will be adjusted to give a beam spot size of at least 10 mm^2 at the diamond to avoid overheating. The quadrupoles will also be adjusted to give a small waist at the position of a collimator located upstream of the detector in ESA. We expect that the beam spot will be about 5 mm tall at the waist, and about 1.5 mm wide due to the increased emittance from synchrotron radiation in the A-line. We have verified that the desired optics can be obtained without quadrupoles Q30 and Q38, which will be positioned after the goniometer and not used in this experiment.

Tuning of the electron beam spot size will be done by sending the electron beam at low repetition rate (10 Hz or less) and low current into End Station A and using the beam position monitors, screens, and SEM wire array built for E158.

To obtain photon beams, the electrons will be bent into a dump using the existing B33-36 dipole magnets, which will need to be refurbished for this experiment. Just upstream of B33, we plan to place a weak magnet with a total field strength of 0.1 kG-m. This bends 48.5 GeV electrons by 0.2 mr. The purpose of the initial soft bend is to minimize the number of energetic synchrotron radiation photons impinging upon the target 110 m downstream. The B33-B36 dipoles are not strong enough to bend electrons with $E > 25$ GeV into the existing high power dump. Therefore we will move the magnets to accommodate a smaller bend angle, and use a smaller 20 kW dump for the electrons. This will require modifying the vacuum chambers of the magnets.

3.3 Photon Beam in End Station A

After entering the End Station, the beam passes through a 3 mm diameter, 70 r.l. tungsten collimator to limit the transverse position and angle of the photons. About 60% to 90% of the photons will hit the collimator (depending on steering), corresponding to a maximum power into the collimator of 20 W for the 0.07% r.l. diamond radiator. A four-quadrant, tungsten pin-cushion shower-emission detector as used in E78 [54] will be placed just in front of the collimator, and the beam will be centered by matching the signals in the left/right

and up/down pairs.

Assuming that the existing E158 spectrometer magnet setup is in place, we plan to place the collimator between the D2 and D3 magnets. The E158 D3 dipole magnet will be powered to provide a sweeping field of 36 kG-m. This magnet will sweep charged particles produced in the collimator by an angle of at least 30 mr. A thick lead wall just in front of the target, with a 1 cm hole for the photon beam, will be used to absorb charged and neutral particles not already absorbed by quadrupoles Q1-Q4. Sufficient shielding in the horizontal plane will be used to prevent muons from the collimator from the reaching the spectrometer detectors.

Electron Energy (GeV)	45.3	48.3	51.3
Electron Current (10^{10}/spill)	2.0	2.0	2.0
Peak Photon Energy (GeV)	35.0	40.0	45.0
Circular Polarization	0.75	0.80	0.84
High p_t Muons/day	160,000	140,000	120,000
days (at 120 Hz, 100% efficiency)	9	10	11

Table 2: Summary of the beam parameters at the three beam energies. The average circular polarization assumes an electron beam polarization of 0.85. The rate per day of muons from open charm with is for $P > 5$ GeV and $p_t > 0.5$ GeV. The rates assume a 0.07% r.l. diamond, 3 mm diameter photon collimator, a 3 cm LiD target, and acceptance for the spectrometer described below. The running time is the total for both absorber configurations.

The photon beam, after passing through the target and muon spectrometers, will be finally stopped in a Secondary Emission Quantameter (SEQ), used to measure the total photon beam intensity, which is energy-weighted flux. Just upstream of the SEQ we will use two auxiliary detectors to monitor the beam flux: an ionization chamber and an atmospheric gas Čerenkov detector. All of these standard devices will be similar to those used in E78 [51].

As in E78 and at Mainz, the goniometer angles will be calibrated by mapping out the ratio of flux (number of photons) compared to intensity as a function of horizontal and vertical angles. Maxima in the ion chamber to SEQ ratios occur at well-defined settings due to channelling radiation, and can be used to determine the correct orientation of the crystal for the desired experimental settings [55, 51, 52].

3.4 Calculations of Photon Beam Flux and Polarization

We have calculated the photon beam flux and intensity profile using the formulas given in Eq. 35 of Ref. [56], as implemented in a Monte Carlo simulation following the very clear introduction to the practicalities of coherent bremsstrahlung given in [57]. We use the same crystal orientation as in [51] for the present calculations. For each electron beam energy, we adjust the angle θ_0 such that the discontinuity (spike) of the lowest energy coherent peak is at a value of k_0/E between 0.77 and 0.88. With no collimation, there is a long tail

extending to lower energies. This tail is reduced by the collimator, as originally proposed in Ref. [58]. The incoherent tail is also reduced by collimation, but in this case the reduction is independent of photon energy. A Monte Carlo program was used to fold in the effects of multiple scattering in the radiator, beam emittance, crystal mosaic spread, and beam spot size as a function of energy. The code was checked against spectra measured in [51], and gives very good agreement with these data. The calculated intensity spectra for the three electron beam energies are shown in Fig. 15. The incoherent contribution is shown as the dashed line. In addition to the main spike, smaller spikes at higher energies are always present in a well-defined intensity ratio.

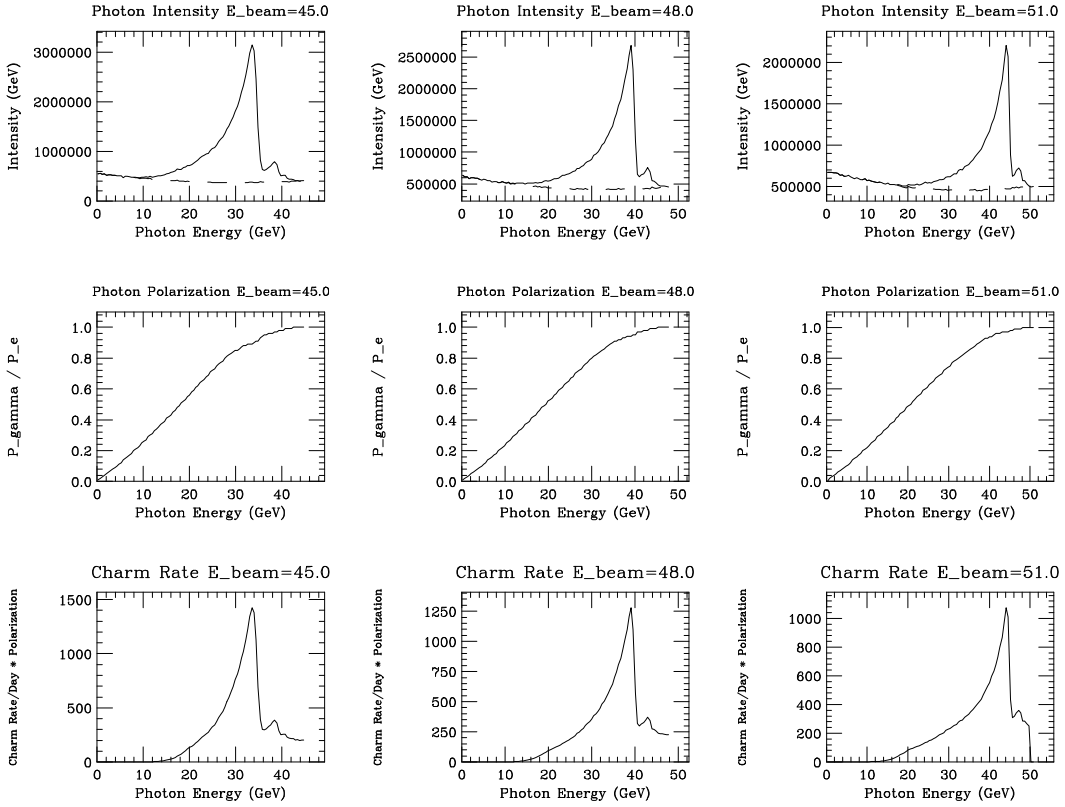

Figure 15: Upper plots are the calculated intensity (flux times energy) for collimated coherent bremsstrahlung at the three setting detailed in Table 2. The dashed lines are incoherent radiation only, while the solid lines include coherent contributions. The middle row of plots show the relative photon circular polarization as a function of photon energy. The lower plots show the corresponding rate per day of muons from open charm with $P > 5$ GeV and $p_t > 0.5$ GeV, scaled by the photon circular polarization.

3.5 Measurements of Photon Beam Flux and Polarization

We will measure the photon flux as a function of energy using pairs of Bethe-Heitler muons produced in the target and measured in our detectors. Using the formulas of [49], we find

that the rate is completely dominated by elastic and quasi-elastic production, for which the sum of the muon energies is equal to the photon energy. We will detect about 10^8 muon pairs per day, so that the statistical error will be very small. The spectrometer momentum resolution is sufficient to resolve the coherent photon peak from incoherent bremsstrahlung. Small corrections will be made for muon pairs from decays of mesons (η, ρ, and ϕ...).

The circular polarization of bremsstrahlung from crystals has been calculated in Ref. [59], and in the reasonable approximation that the two ψ_2 terms are equal to the corresponding coherent and incoherent ψ_1 terms, is simply given by

$$P_\gamma = P_e \frac{1-(1-y)^2-\frac{2}{3}y(1-y)}{1+(1-y)^2-\frac{2}{3}(1-y)} = P_e \frac{y(4-y)}{4-4y+3y^2},$$

where $y = k/E$. In this approximation, the polarization is the same for the coherent and incoherent components. A more exact treatment includes the effects of linear polarization for the photons in the coherent peaks. The degree of linear polarization is maximal at low photon energies, decreasing to zero at the highest photon energies. This trend is opposite to that for circular polarization. The net result is that the photons will be elliptically polarized. The results of the full calculation for the circular polarization as a function of photon energy are shown in the middle panels of Fig. 15 for photon spectra in the top panels. It can be seen that the average circular polarization increases strongly with k/E. The small dips visible at the coherent peak positions are due to the relatively small linear polarization components at our chosen kinematics. The average circular polarization (weighted by the open charm cross section) is given in Table 2.

We note that the effect of 5% to 20% linear polarization of the photons will cancel in the measurement of $\Delta g(x)$, because the orientation does not depend on the electron beam helicity, which is flipped randomly from pulse to pulse. In addition, the azimuthal symmetry of our detector will cancel out effects in the total rates.

We plan to measure the product of beam and target polarization using the large sample of Bethe-Heitler muon pairs that will also be used to monitor the total flux. The cross section asymmetry has recently been calculated [60], and depends on the known spin structure functions g_1 and g_2. Specific kinematic cuts will be used to emphasize the region where the expected asymmetries are large. Our initial estimates indicate that sufficient statistics will be obtained to measure the product of beam and target polarization to better than 8%. As a check, we will also measure the electron beam polarization using the E158 setup and calculate the photon beam polarization. The target polarization will also be separately measured.

4 Polarized Target

The target will be a 3 cm long, 1 cm diameter cylinder filled with ^{6}LiD , which is polarized using the technique of Dynamic Nuclear Polarization (DNP). Using a dilution refrigerator at 300mK, in conjunction with a magnetic field of up to 6.5 T, we expect 70% polarization [62] for the deuteron and ^{6}Li. The setup will be similar to that used in SLAC experiments E143 and E155 [61].

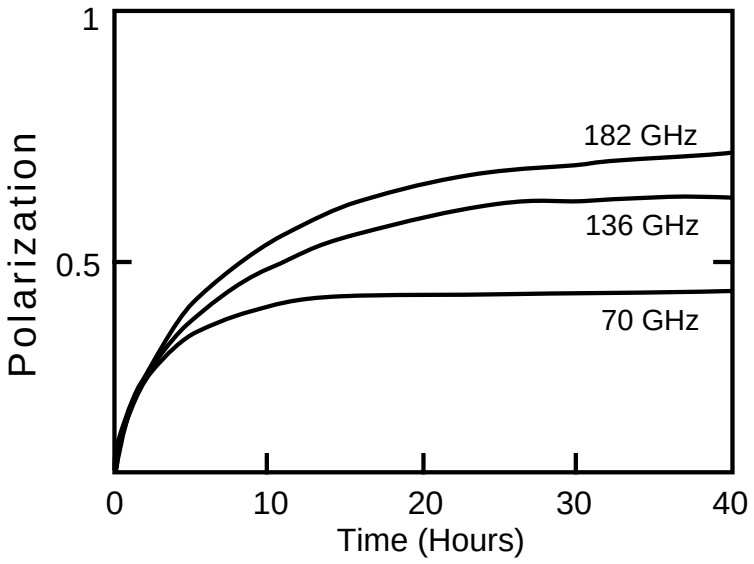

Figure 16: Polarization of ^{6}Li measured by Abragam et al as a function of time for three combinations of field and frequency. The upper curve corresponds to 6.5 T, close to the conditions of this proposal. The middle curve corresponds to about 4.9 T.

4.1 Target Material

The 3 cm long ^{6}LiD target corresponds to about 1 gm/cm^2 of material, or 1.1 b^{-1} and is about 2% of a radiation length. Various studies have shown that, to a good approximation, ^{6}Li acts as a polarized proton and a polarized neutron plus an unpolarized spectator α-particle [63]. This results in a spin dilution factor of $f \approx 0.5$ (compared to 0.22 for ND_3), where f is the fraction of polarizable nucleons in the target. Even after taking into account target windows and liquid helium, $f \approx 0.4$, and in conjunction with its high polarization, ^{6}LiD gives a much higher nucleon average polarization than any other solid target. LiD polarized targets have been successfully used by the University of Virginia group to measure g_1 [5], and g_2 at SLAC and will be used by COMPASS.

^{6}LiD must be preirradiated to create the paramagnetic centers necessary for DNP. Abragam and colleagues at Saclay [62, 64] were the first to polarize it and obtained 70% for ^{6}Li at a magnetic field of 6.5 T and a temperature of ~300 mK (see Fig. 16). Lower polarizations were obtained at lower fields (64% at 4.9 T; 40% at 2.5 T). The polarizing times are long (~20 to 40 hours), but 70% of the final polarization can be obtained in about 10 hours. Further studies at Saclay [65] and investigations at Bonn [66] and PSI [67] have confirmed the ability to reach high polarizations after a few hours of polarizing.

4.2 Magnet and Microwaves

The solenoid used in E143 and E155 is unlikely to be available, so we plan to use a new solenoid capable of operating at fields up to 7 T. The coils are large enough so that all particles leaving the target at angles less than 20 degrees reach the detectors without

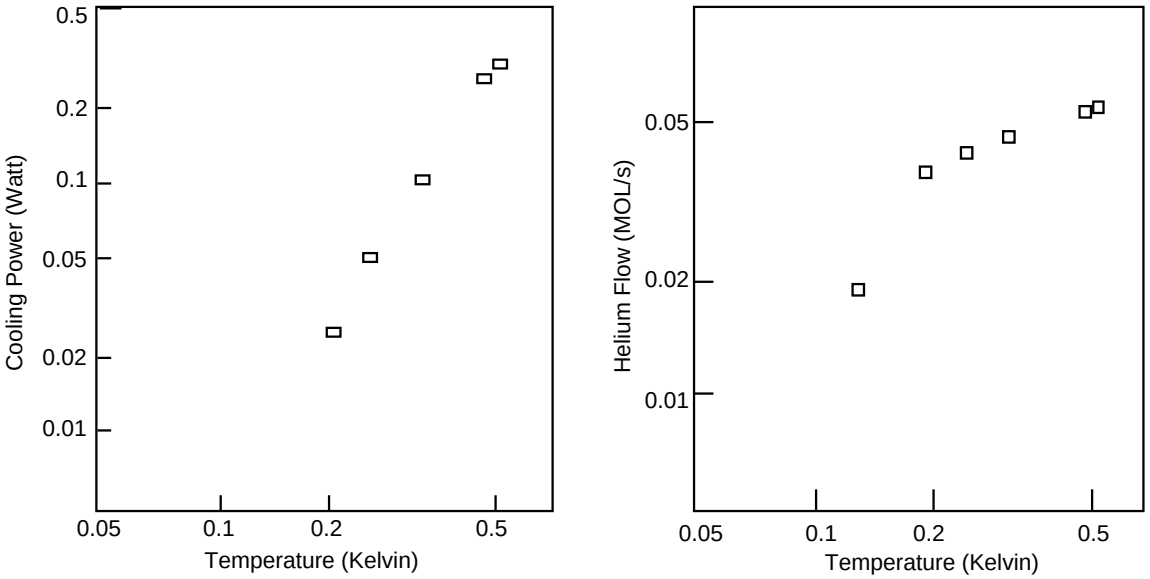

Figure 17: Cooling power for the refrigerator of this proposal (open squares) as a function of temperature. The relation between temperature and helium flow is also shown.

hitting coils or other thick materials. Oxford Instruments has a design which can be slightly modified to meet our needs. It will have a uniform field region of 5 cm and a 20 cm warm bore for our shielding. The field that we run at will depend on the availability of microwave power sources of the appropriate frequency, but will be in the range 6 to 6.5 T. Running above 6 T may require additional equipment.

4.3 Refrigerator

The requirement is for a high power dilution refrigerator with at least 200 mW of cooling power at 300 mK. The University of Virginia polarized target group have such a refrigerator which was obtained from CERN. This dilution refrigerator was operated as a target material test facility and was described by Niinikoski and Rieubland [68]. The important features of this refrigerator are: rapid cold access to the mixing chamber for target material changes; fast evacuation and cool down; horizontal operation allowing the beam to go down the axis with minimal material in the way. Figure 17 shows the cooling power performance of this refrigerator. There is potential for improvement as it was originally designed for a circulation rate of 100 mmole/sec but was only operated at up to 60 mmole/sec. However at one point the mixing chamber was modified for another application, so it will have to be unmodified and redesigned to accommodate the size of the target holder. But as described in Ref. [68] it is well matched for DNP of ^{6}LiD. A large fraction of the heat input to the mixing chamber comes from the microwaves (100 to 200 mW) while the beam contributes no more than about 10 mW.

In summary, the polarized target will use irradiated ^{6}LiD in a dilution refrigerator operating at 300 mK, together with a superconducting warm-bore solenoid at $\leq$ 6.5 T.

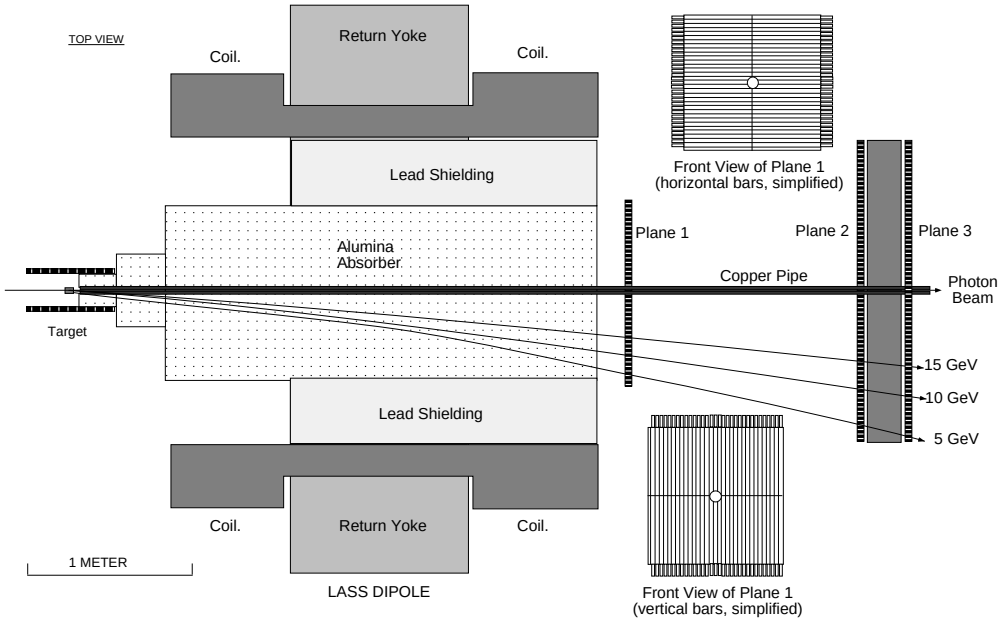

Figure 18: Overall plan view of the main components of the spectrometer. The absorber fills most of the gap of the LASS dipole, and also extends into the warm bore of the target magnet. A thick evacuated copper beam pipe contains the photon beam. The three detector planes are made from scintillator hodoscopes. Two simplified front views of the front plane are shown. The dashed curves are typical trajectories for muons with $p_t = 0.7$ and $P = 5$, 10, and 15 GeV.

5 Spectrometer, Detector and Electronics

5.1 Introduction

The challenge is to identifying thousands per day of high p_t muons from open charm decay amongst the approximately 1000 times higher rate of pions and kaons from typical hadronic interactions in the target. We propose to achieve this goal using the detector shown in Fig. 18. Absorbers are placed very close to the target with enough interaction lengths and radiation lengths to almost completely contain all hadronic and electromagnetic showers. The amount of absorber needed is reduced somewhat by placing the material in a magnetic field, which is also used to determine the momentum of the muons.

5.2 Absorber

We plan to absorb most photoproduced hadrons and photons primarily using alumina (aluminum dioxide, Al_2O_3) placed just downstream of the target. The closer to the target, the fewer the number of muons from pion and kaon decays. Alumina was chosen because of the relatively low number of radiation lengths per interaction length, affordable cost, and its high density. For the background estimates we have used commercially available

alumina bricks with a density of 3.6 gm/cc, and 90% purity (the remainder is mainly silicon dioxide).

Studies with GEANT indicate that a length of 3 m of alumina outside of a 6 to 8 cm diameter copper pipe around the beam line is sufficient to meet our goal of reducing the rate of charged particles from punch-through of hadronic and electromagnetic showers to a level below that of muons. The copper pipe has the effect of increasing the number of interaction lengths and radiation lengths for the numerous small angle Bethe-Heitler electron and muon pairs and thus attenuating these particles more than the wider angle muons from open charm decay. The inner diameter of the copper pipe will be made as small as possible consistent with an acceptable level from tails in the photon transverse distribution (about 2 cm diameter).

The magnetic field in the dipole in Fig. 18 reduces the total amount of absorber needed, because low momentum secondaries curl up the field and are soon ranged out. The GEANT studies show a higher rate of photons and neutrons hitting the front detector plane, compared to charged particles, but scaled by their detection efficiency, the singles rates will still be dominated by the charged particles.

In order to measure the rate and asymmetry of muons from pion and kaon decays, we will also take data with an absorber configuration that increases the fraction of high p_T muons from these decays by about a factor of five. This configuration, shown in Fig. 19, has the alumina removed, to be replaced by a 1.4 m thick copper wall beginning about 2 m from the target.

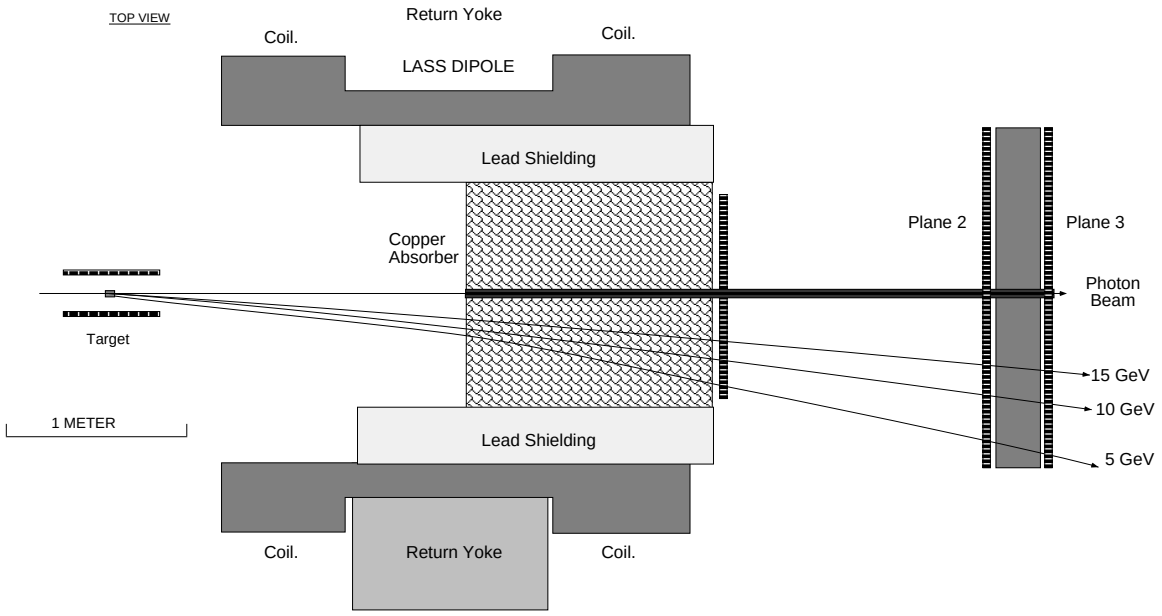

Figure 19: Plan view of the spectrometer with the absorber configuration that enhances the rate of muons from pion and kaon decays .

5.3 Spectrometer

The spectrometer layout is shown in Fig. 18. The dipole is the 70D43 LASS dipole [70] oriented to bend in the horizontal direction. This dipole has two very large sets of coils arranged in a configuration that limits the useful vertical(non-bend plane) opening to about ± 55 cm over the 2.8 m distance between the mirror plates. The pole face is 109 cm long, and the gap is 102 cm. We plan to add shims to reduce the gap to about ± 45 cm to match the acceptance to that determined by the magnet coils, and to get a higher integrated field. With two existing 1.6 MW supplies in parallel running at 2000 amps each, we expect to obtain an integrated field strength of 25 kG-m. The mirror plates will be left on to reduce the field gradient at the polarized target and at the position of the front detector phototubes.

The three dashed lines on Figs. 18 and 19 show the trajectories of a typical muons with $p_T = 0.7$ GeV, at momenta of 5, 10, and 15 GeV.

The spectrometer can be calibrated by using the approximate 10^5 J/ψ events.

5.4 Detectors

Tracking of the muons will be done using planes of scintillator hodoscopes. The fine granularity and good timing of this type of system are needed to match hits from muon tracks that will occur on average every 15 to 25 nsec. We plan to use three planes of hodoscopes as seen in Fig. 18. The first two planes have fine resolution for measuring momentum and angles, while the last plane, shielded behind additional lead, has less granularity and will be used to establish a point in space and time on the muon track at a location where the singles rates are much lower. The planes are segmented into top and bottom halves for the horizontal measuring readout (vertical fingers), and left and right halves for the vertical measuring readout (horizontal fingers). This is done to reduce the random hit rate per finger, and to reduce the spread in signal height from attenuation of the light in the scintillator.

The first two planes will be highly segmented. For horizontal positions (bend plane) each of the first two planes of vertical fingers will be divided into two overlapping sub-planes with 1.5 cm average finger width. This gives an effective resolution of 0.2 cm. Each sub-plane will have full coverage, so that a good muon can be required to fire fingers in both sub planes. This is done to reduce accidental hits from background neutrons and photons. The finger widths will be smaller near the beam line and larger farther away, corresponding to high and low momentum muons respectively. Vertical positions (non-bend plane) will be measured with horizontal fingers, each with 2 cm width, but with only a single sub-plane per plane, giving a position resolution of 0.7 cm. This gives a vertical angle resolution that is good enough to distinguish muons originating from the target from most random background from hadronic interactions in the absorber. The third plane will have a single layer of horizontal measuring fingers. Each finger will be approximately 5 cm wide. Table 3 lists the overall dimensions of each plane, as well as the number of hodoscope fingers needed.

We plan to read out each finger with small PMTs, most of which can be taken from the existing E155 hodoscope arrays. The front plane will be 20 cm beyond the LASS dipole

Plane	x (cm)	y (cm)	fingers
1	± 55	± 55	350
2	± 90	± 75	555
3	± 100	± 85	80
Total			985

Table 3: Dimensions of each scintillator plane and number of fingers.

mirror plate, where adequate magnetic shielding can be fabricated. The signals from each hodoscope will pass through a discriminator and into a multi-hit TDC with 0.5 nsec bin size and leading edge readout. A similar system of scintillator hodoscopes was used in recent experiments E154 and E155. The experience with that system indicates that the proposed system will be able to reliably track an expected rate of about 20 to 30 muons per beam spill, in the presence of an expected random sprinkle hit rate of less than 1 hit per finger per plane. This is a total of less than 2000 TDC hits per spill.

5.5 Acceptance and Resolution

A simple model of the spectrometer has been used to determine the expected performance. The effects of multiple scattering in the absorber and detectors, energy loss (and fluctuations) in the absorber, photon beam size, target length, and detector granularity have been taken into account. A realistic sample of muons at momenta of 5, 10, and 15 GeV were swum through the system. A summary of the results is shown in Table 4.

P	5	10	15
P Resolution (GeV)	.717	1.542	2.641
θ Resolution (rad)	.015	.008	.005
p_T Resolution (GeV)	.092	.117	.145
Acceptance for $p_T > 0.5$ GeV	.330	.863	.999

Table 4: Acceptance and resolutions expected at each of the primary photon energies.

The acceptance for the muons of interest $p_T > 0.5$ GeV increases from about 0.33 at 5 GeV to near 100% at 15 GeV. Averaged over all momenta, about half of all high p_T muons from open charm decay will be detected. Muons in the open charm acceptance region that are from Bethe-Heitler pair production are rejected at the 85% level by detecting the second muon. This other muon is usually produced at a small angle, where the acceptance is very good. If there is a second muon from J/ψ decay, the acceptance is somewhat lower, averaging approximately 75%.

The principal requirement for resolution is that p_T be measured to better than 0.15 GeV, so that open charm muons can be separated from background muons using the difference in p_T dependence. The proposed spectrometer meets this requirement at 15 GeV, and exceeds it at lower momenta. Folding the spectrometer resolution with a realistic p_T distribution

indicates that in the worst case the ratio of background to signal will be increased by 20% due to resolution effects.

The momentum resolution is good enough so that the coherent photon peak can be observed using the energy sum of Bethe-Heitler muon pairs. The angular resolution gives the necessary resolution on the invariant mass and transverse momentum of the pair used for kinematic cuts for the polarization measurements. The mass resolution near the J/ψ peak is about 0.4 GeV, adequate to resolve J/ψ decays from Bethe-Heitler pairs.

6 Results

The anticipated statistical precision of the experiment is shown in Fig. 20 for the three peak energies of the beam and two different muon momentum ranges. The data points are shown at the arbitrary value of zero, with the errors expected from the experiment. The error estimates include the corrections due to pion and kaon decay and those due to associated production. The errors are as small as 0.012 on the asymmetry over many data points at different energies and t_T^μ. The predicted asymmetry using representative fits as in Fig. 4 are shown here. Our experiment can easily distinguish between them. Averaging over the points will give an error of about 0.006 at each of the energies as seen in Fig. 21. To determine $\Delta g(x)$ in a model independent way, we must deconvolute Eq. 4 taking into account the kinematics of charm decay into muons. This large, but straightforward, task awaits approval of the experiment.

7 Request to SLAC

We request two weeks of checkout at low repetition rate and two months of running at a linac repetition rate of 120 Hz (or four months at 60 Hz). This assumes that the run takes place between PEP-II fills with an average data collection efficiency of 50%. The running time will be divided approximately equally among beam energies of 45, 48.3, and 51.3 GeV. We request the re-establishment of the polarized photon beam capability as used in E78. This will involve re-installation of the goniometer, refurbishing the dump magnets, installing a small beam dump, and help in re-establishing the standard photon beam monitors. Additional diamonds will be supplied by the collaboration (Yerevan) if needed. We request the use of the LASS dipole with a reduced gap between the pole faces. We request resources to purchase the hodoscope scintillator fingers, with assembly planned to be done by the collaboration. We will need to increase the existing supply of PMT channels to read out the hodoscopes by several hundred. Most of the needed discriminators and TDC's are already available. Some upgrades to the E.S.A. DAQ system may be needed to handle an estimated data rate of up to 2000 TDC hits per spill.

The collaboration will provide many of the target components, such as the dilution refrigerator, target material, and diagnostic equipment. We request that SLAC acquire equipment needed to run at higher target magnetic fields than the previous E.S.A. experiments, primarily a higher frequency microwave assembly, and a 7 T target magnet.

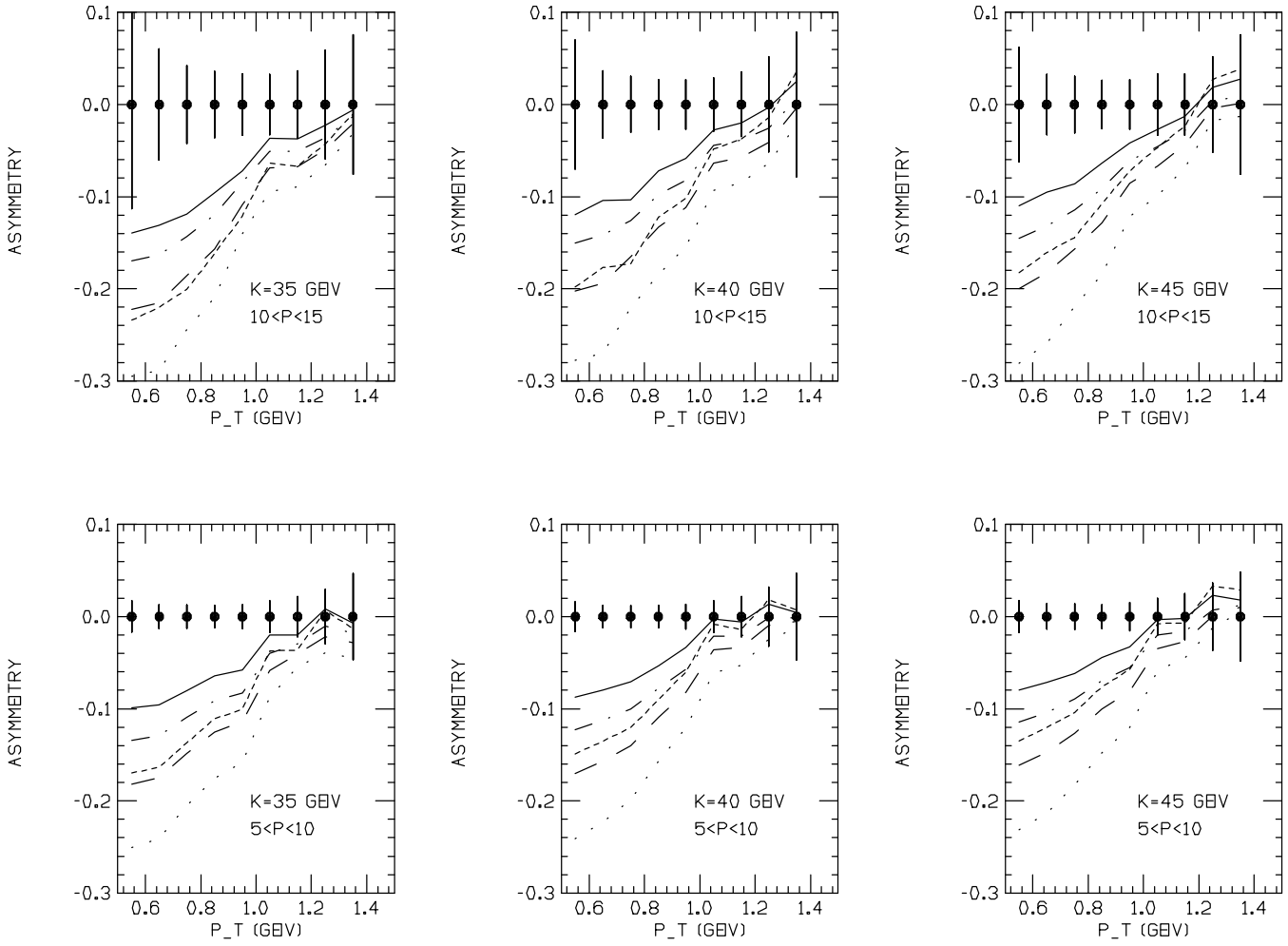

Figure 20: Asymmetries for the five fits to the gluon polarization of Fig. 4 as a function of p_T^μ of the detected muon. The top row is for $10 < P_\mu < 15$ GeV and the bottom row for $5 < P_\mu < 10$. The three columns correspond to peak beam energies of 35, 40 and 45 Gev. The points indicate the projected statistical errors for the running conditions given in the text. Experimental systematic errors will be highly correlated from point-to-point, and will be approximately 0.10 of the measured asymmetries.

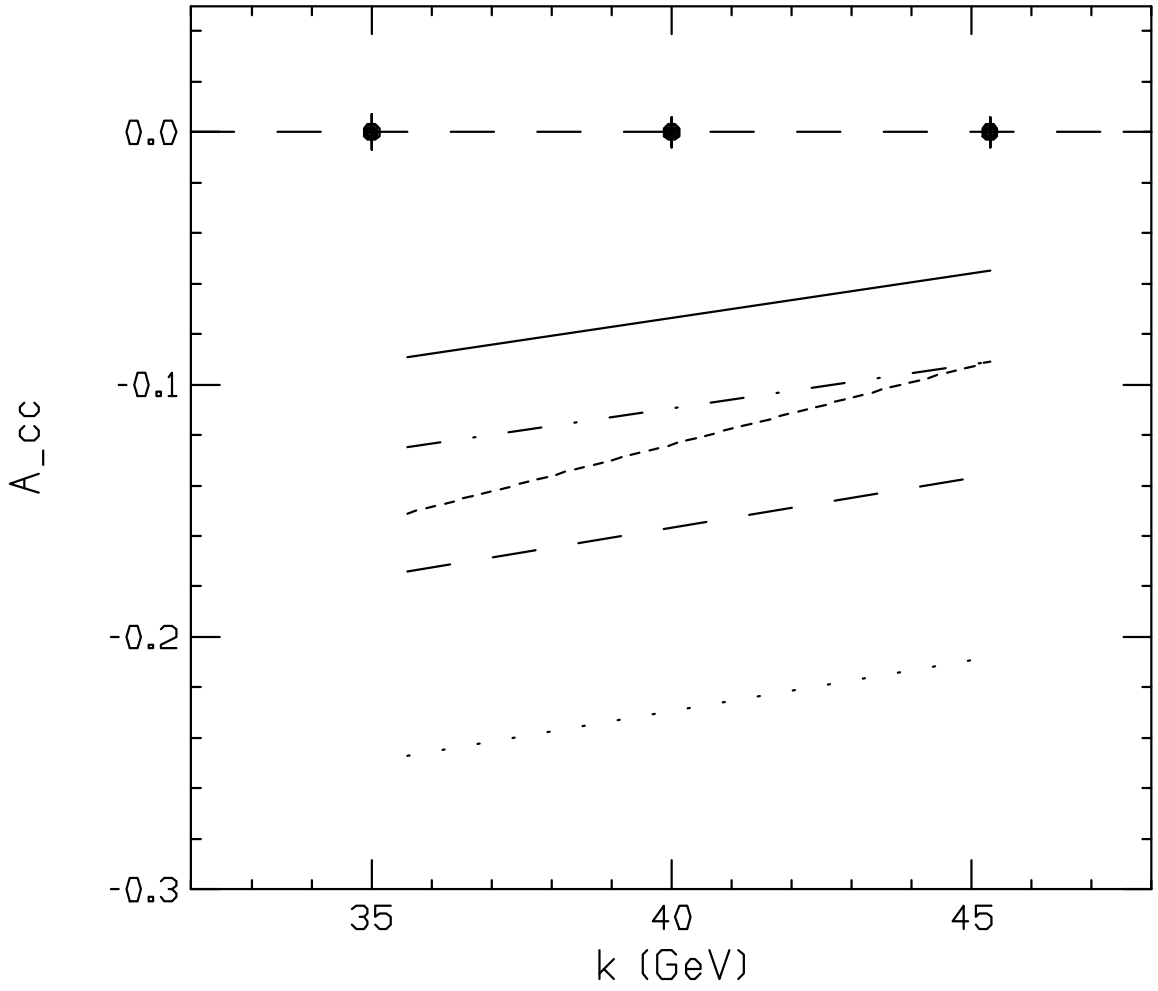

Figure 21: Asymmetries for the five fits to the gluon polarization of Fig. 4 as a function of beam energy. The points, arbitrarily placed at zero asymmetry, indicate the projected statistical errors for the running conditions given in the text, averaged over p_T.

Acknowledgments

We thank V. Breton, S. Brodsky, R. Gardner, D. Pierce, E. Quack, T. Sjostrand, R. Vogt, and many others for useful discussions and other assistance.

References

[1] SLAC E142, P. L. Anthony *et al.,* hep-ph/0007248.

[2] SLAC E143, K. Abe *et al.,* Phys. Rev. Lett. **74** (1995), 346.

[3] SLAC E143, K. Abe *et al.,* Phys. Rev. Lett. **75** (1995), 25.

[4] E154 Collaboration: K. Abe *et al.*, Phys. Rev. Lett. **79**, 26(1997),

[5] E155 Collaboration: P. Anthony *et al.*, Phys. Lett. B **463** (1999) 339.

[6] E155 Collaboration: P. Anthony *et al.*, hep-ph/0007248

[7] G. Altarelli and G. Parisi, Nucl. Phys. **B126** (1977), 298; V. N. Gribov and L. N. Lipatov, Yad. Fiz. **15** (1972), 781 [Sov. J. Nucl. Phys. **15** (1972), 438].

[8] J. D. Bjorken, Phys. Rev. **148** (1966), 1467; Phys. Rev. D **1** (1970), 1376.

[9] EMC, J. Ashman *et al.,* Phys. Lett. **B206** (1988), 364; Nucl. Phys. **B328** (1989), 1.

[10] SLAC E155, P. L. Anthony *et al.,* Phys. Rev. D **54** (1996) 6620.

[11] J. Ellis and R. Jaffe, Phys. Rev. D 9 (1974), 1444; D **10** (1974), 1669 (E).

[12] G. Altarelli and W. J. Sterling, Particle World 1(2), **40** (1989); G. Altarelli and G. G. Ross, Phys. Lett. B212,**391** (1988).

[13] E. B. Zijlstra and W. L. van Neerven, Nucl. Phys. **B417** (1994), 61; R. Mertig and W. L. van Neerven, Z. Phys. **C70**, 637 (1996) and INLO-PUB-12-95, September 1995.

[14] M. Glück, E. Reya, M. Stratmann, and W. Vogelsang, HEP-PH/9910318; Phys. Rev. D **53** (1996) 4775.

[15] B. Aveda *et al.,* Phys. Rev. **D58** (1998) 112002.

[16] G. Altarelli,R. D. Ball, S. Forte, and G. Ridolfi, hep-ph/9803237.

[17] S. J. Brodsky, M. Burkardt, and I. Schmidt, Nucl. Phys. **B441** (1995), 197.

[18] T. Gehrmann and W. J. Stirling, Phys. Rev. D **53** (1996) 6100.

[19] M. Glück, E. Reya, M. Stratmann, and W. Vogelsang, Phys. Rev. D **53** (1996) 4775.

[20] R. D. Ball, S. Forte, and G. Ridolfi, Phys. Lett. **B378** (1996) 255.

[21] R. L. Jaffe, Phys. Lett. **B365**, 359 (1996).

[22] I. I. Balitsky, V. M. Braun and A. V. Kolesnichenko, Phys. Lett. **B242** (1990), 245; **B318** (1993), 648 (E); X. Ji and P. Unrau, Phys. Lett. **B333** (1994), 228; E. Stein, P. Cornicki, L. Mankiewicz, A. Schafer, Phys. Lett. **B353** (1995), 107.

[23] D. L. Adams *et al.*, Phys. Lett. **B336**, 269 (1994).

[24] HERMES Collaboration, A. Airapetian *et al.*, hep-ex/9907020.

[25] Stan Brodsky, Private communication.

[26] G. Bunce *et al.*, Particle World 3,**1** (1992).

[27] M. Gluck and E, Reya, Z. Phys. **C39**, 569 (1988).

[28] S. Keller and J. F. Owens, Phys. Rev. D **49** (1994) 1199.

[29] I. Bojak and M. Stratmann, Phys. Lett. **B433** (1998) 411; Nucl. Phys. **B540** (1999) 345; Erratum: ibid **B569** (2000) 694.

[30] Z. Merebashvili, A.P. Contogouris, G. Grispos, hep-ph/0007050.

[31] J. Smith and W. L. van Neerven, Nucl. Phys. **B374** (1992) 36. R. K. Ellis and P. Nason, Nucl. Phys. **B312** (1989) 551.

[32] COMPASS proposal, CERN/SPSLC -96-14 (March, 1996).

[33] M Amarian *et al.,*, DESY-PRC97/03 (January, 1997).

[34] J. J. Aubert *et al.,* Nuc. Phys. **B213**, 31 (1983).

[35] S. Frixione and G. Ridolfi, hep-ph/9605209 (May, 1996).

[36] M. Fontannaz, B. Pire, and D. Schiff, Z. Phys. **C11**, 211 (1981).

[37] J. C. Anjos *et al.,* Phys. Rev. Lett. **65**, 2503 (1990).

[38] G. Marchesini, B. R. Webber, G. Abbiendi, I. G. Knowles, M. H. Seymour and L. Stanco, Computer Phys. Commun. **67** (1992) 465; hep-ph/9912396.

[39] T. Sjostrand, Computer Physics Commun. **82**, 74 (1994).

[40] K. Abe *et al.*, Phys. Rev. D**33** (1986) 1.

[41] M. P. Alvarez *et al.*, Z. Phys. C**60** (1993) 53.

[42] P. L. Frabetti *et al.* Phys. Lett. B**370** (1996) 222.

[43] D. Wiser, PhD thesis, University of Wisconsin, 1977 (unpublished).

[44] D. Ritson, SLAC-PUB-1728 (1976), published in Nashville Conf. 1976:75.

[45] The E155 Collaboration, P.L. Anthony *et al.,* Phys. Lett. **B458** (1999) 536.

[46] A. Afanasev, C. E. Carlson, C. Wahlquist, Phys. Rev. **D 61** (2000) 341014.

[47] S.D. Bass and M.M. Brisudova, Eur. Phys. J. **A4** (1999) 251.

[48] E. Thomas, N. Bianchi,Nucl. Phys. Proc. Suppl. **82** (2000) 256.

[49] Y.S. Tsai, Rev. Mod. Phys. **46** (1974) 815; **49** (1977) 421 (E).

[50] R. Yoshida, Nucl. Instrum. Meth. **A302** (1991) 63.

[51] W. Kaune *et al.*, Phys. Rev. D **11**, 478 (1975).

[52] D. Lohmann *et al.*, N.I.M. **A343** (1994) 494.

[53] R. Schwitters, SLAC-TN-70-32 (1970).

[54] G. Miller and D. Walz, SLAC-PUB-1297.

[55] D. Luckey and R. Schwitters, Nucl. Instrum. Meth. **81**, 164 (1970).

[56] G. Diambrini Palazzi, Rev. Mod. Phys. **40**, 611 (1968).

[57] R. Jones, http://zeus.phys.uconn.edu/halld/cobrems-7-97/

[58] R. F. Mozley and J. DeWire, Nuevo Cimento **27**, 1281 (1983).

[59] I. M. Nadzhafov, Bulletin of the Academay of Sciences of the USSR, Physical Series Vol 14, No. 10, p. 2248 (1976).

[60] T. Gehrmann, M. Stratmann, Phys. Rev. **D56** (1997) 5839.

[61] T.D. Averett *et al.,* Nucl. Instrum. Meth. **A427** (1999) 440.

[62] A. Abragam *et al.*, J. Physique - Letts., **41**, L-309 (1980).

[63] N. W. Schellingerhout *et al.*, Phys. Rev. C **48,** 2714 (1993).

[64] V. Bouffard *et al.*, J. Physique, **41**, 1447 (1980).

[65] G. Durand *et al.*, Proc. Int. Symp. on High Energy Spin Physics, Nagoya, Japan 1992, eds. T. Hasegawa *et al.,* p. 355.

[66] S. Goertz *et al.*, Nucl. Instrum. Meth. in Phys. Res., **A356**, 20 (1995).

[67] B. van den Brandt et al., Proc. 9th High Energy Spin Physics Symp. Bonn, Germany, 1990, p. 320.

[68] T. Niinikoski and J. Rieubland, Proc. Ninth Cryo. Eng. Conf., Kobe, Japan, 1982, p. 580.

[69] D.O. Caldwell *et al.,* Phys. Rev. **D7** (1973) 1362.

[70] SLAC Report 298, April 1986.